Active Nanophotonic Circuitry Based on Dielectric-loaded Plasmonic Waveguides

Alexey V. Krasavin* and Anatoly V. Zayats

Surface plasmon polaritons provide a unique opportunity to localize and guide optical signals on deeply subwavelength scales and can be used as a prospective information carrier in highly integrated photonic circuits. Dielectric-loaded surface plasmon polariton waveguides present a particular interest for applications offering a unique platform for the realization of integrated active functionalities. This includes active control of plasmonic propagation using thermo-optic, electro-optic, and all-optical switching as well as compensation of propagation losses. In this review, the principles and performance of such waveguides are discussed and the current status of the related active plasmonic components which can be integrated in silicon or other nanophotonic circuitries is summarized. A comparison of dielectric-loaded and other plasmonic waveguides is presented and various material platforms and design pathways are discussed.

1. Introduction

Optical signals have undisputable advantage over electronic ones for data transmission, providing incomparably higher data transfer rates and enabling modern communications technologies. The implementation of optical communication principles on the nanoscale and integrating nanophotonics into electronic circuitry can in turn boost data transfer rates between and within electronic chips. This will resolve the problem of the electronic interconnect bottleneck which impedes the development of modern electronic chips and circuitry due to inability of nanosacle electric conductors to provide high bandwidth.[1–3] Furthermore, optical data processing can occur at much faster rates in comparison with the characteristic speeds in the modern electronics,[4–6] which creates a potential for the development of ultra-fast switching and routing optoelectronic components. These ideas of integrating optical data circuits in the existing electronic chips or even the development of all-optical information-processing in integrated circuits stumble however at the problem of size of photonic waveguides and components: due to the diffraction of light, the optical signal cannot be localized in a region of space much less than approximately $\lambda/2n$, where λ is the wavelength of light and n is the refractive index of the waveguide material. Therefore, with all the advantages of conventional photonic circuits, their integration level has

one to two orders of magnitude mismatch with that of electronic chips: hundreds of nanometers in Si photonics vs. tens of nanometers in modern electronic chips. Nevertheless, one can design photonic components based on metallic nanostructures, the so-called plasmonic components, which can trap optical field by coupling it to free-electron excitations near a metal surface on the length scales comparable to the sizes of electronic interconnects.[7]

1.1. Plasmonics and Nanoscale Optical Circuitry

Plasmonics makes use of coupling between electromagnetic waves and free-electron excitations at the interface between negative permittivity materials such as metals (or degenerate semiconductors) and positive permittivity dielectrics.[8,9] In different geometries, plasmonic excitations manifest themselves as localized surface plasmons (LSPs) supported by metallic nanoparticles[9–12] or propagating surface waves, surface plasmon polaritons (SPPs) on an extended metallic interfaces (e.g., films or nanowires).[7,8,13] Their unique properties associated with high electromagnetic field confinement and consequent field enhancement near the conductor's surface[14,15] have long attracted significant attention in chemical[16,17] and biosensing due to the strong refractive index sensitivity[18,19] as well as surface enhanced Raman scattering.[20,21] Nonlinear optical processes, which are proportional to the higher orders of the electric field, are also dramatically boosted due to the plasmonic field enhancement.[22,23] The examples include the enhancement of Kerr-type nonlinearity,[24–27] harmonic generation,[23,28,29] and four-wave mixing[30] in metal nanostructures and surrounding dielectrics, self-focusing and SPP-soliton formation,[31] and many others. Taking on the above properties, plasmonics offers a unique opportunity to combine the speed and the bandwidth of nanophotonics with the integration level of the electronics[32] and provide superior active functionalities leading to the development on nonlinear nanophotonic components.

Based on this idea, numerous geometries for SPP waveguides have been proposed, covering a broad range of field confinement levels. Due to the presence of the plasmonic field in metal and consequent Ohmic losses, SPP waveguides introduce signal attenuation. Generally, there is a trade-off between these two parameters: the higher the confinement, the larger portion of the electromagnetic field is localized in metal leading to the higher losses and the stronger signal

Dr. A. V. Krasavin, Prof. A. V. Zayats
Department of Physics
King's College London
Strand, London WC2R 2LS, UK
E-mail: alexey.krasavin@kcl.ac.uk

www.MaterialsViews.com

ADVANCED
OPTICAL
MATERIALS

www.advopticalmat.de

REVIEW

attenuation. Long-range surface plasmon polariton modes, supported by thin (typically less than 20 nm) metallic stripes in symmetric environment (**Figure 1**a), have the longest propagation length (defined as the distance after which the intensity drops e times), which can reach centimeter range at the telecommunication wavelengths, paying the price of low confinement (several micrometers) which does not beat dielectric waveguides.[33,34] Such long propagation length is the result of interplay between the plasmonic oscillations at the top and the bottom interfaces of the stripe, resulting in the mode with the electromagnetic fields pushed out of the metal and therefore decreased Ohmic losses. A typical example of the plasmonic modes which broke below the diffraction limit, but still have a reasonably long propagation length (on the order of 100 μm) are channel plasmon polaritons (Figure 1b).[35] Here, the mode in the groove is formed by coupling of the plasmonic oscillations propagating along its opposite sides. Several approaches have been used to localize the plasmonic mode in truly nanoscale dimensions, with typical propagation lengths of tens of micrometers. Metal–dielectric–metal SPP mode (Figure 1c) has the same nature as the channel mode but offers much stronger confinement[36] having no limitation on a dielectric gap thickness (planar waveguides with 3 nm gaps have been experimentally demonstrated).[37] Plasmonic mode propagating along a metallic nanowire[38–40] (Figure 1d,e), which can be considered 1D charge oscillations, has no cut-off: the smaller the wire diameter, the stronger the field confinement. Coupled plasmonic oscillations in metallic nanoparticles arranged to form a chain waveguide, produce a highly localized plasmonic mode (Figure 1f).[41] Significant improvement of guiding characteristics was achieved in hybrid[42] plasmonic waveguides, where the mode is produced by coupling a plasmonic mode with a photonic mode of high refractive index ridge waveguide separated from a metal surface by a low refractive index spacer (Figure 1g). Recently, plasmonic metamaterial-based waveguides have been shown to produce highly confined modes of bulk plasmon–polaritons.[43,44]

Alexey V. Krasavin received his BSc (with honors) and MSc (with honors) degrees from the Moscow Institute of Physics and Technology. In 2006, he received a PhD in Physics from the University of Southampton and joined Queen's University Belfast as a postdoctoral research fellow. Since 2010 he has worked in King's College London. His research interests include the active manipulation and amplification of plasmonic signals in highly integrated optical circuits, nonlinear plasmonic-assisted effects, plasmonic-enhanced fluorescence, and optical metamaterials.

Anatoly V. Zayats is the head of the Experimental Biophysics and Nanotechnology Group at the Department of Physics, King's College London. He graduated and received a PhD in Physics from the Moscow Institute of Physics and Technology. His current research interests are in the areas of nanophotonics and plasmonics, metamaterials, nonlinear optics, and spectroscopy. He is a holder of the Royal Society Wolfson Research Merit Award, a Fellow of the Institute of Physics, the Optical Society of America, SPIE, and The Royal Society of Chemistry.
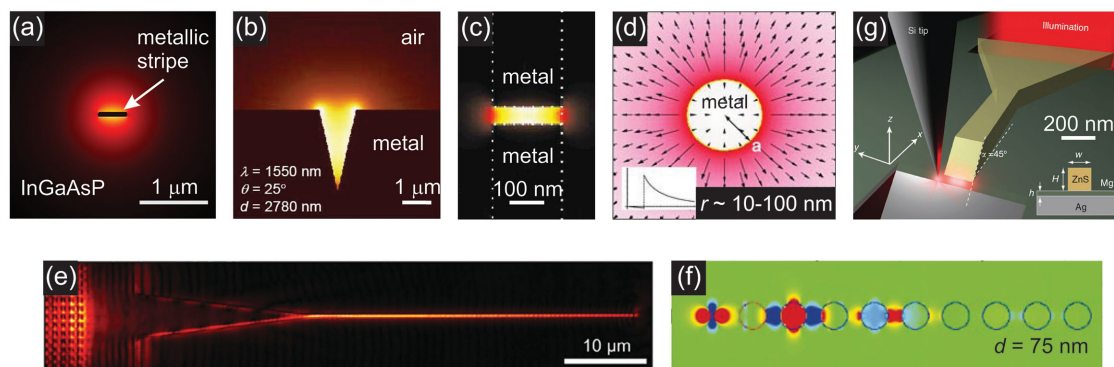
Figure 1. Different types of SPP waveguides. a) Long-range SPP waveguide. Reproduced with permission.[45] Copyright 2004, Optical Society of America. b) Channel SPP waveguide. Reproduced with permission.[46] Copyright 2008, Optical Society of America. c) Metal–dielectric–metal SPP waveguide. Reproduced with permission.[36] Copyright 2005, Optical Society of America. d) SPP mode of a cylindric metallic nanowire. Reproduced with permission.[47] Copyright 2004, Optical Society of America. e) SPP mode coupling and propagation in a metal stripe waveguide. Reproduced with permission.[39] Copyright 2009, The American Physical Society. f) Plasmonic waveguide formed by a chain of metallic nanoparticles. Reproduced with permission.[48] Copyright 2003, The American Physical Society. g) Hybrid plasmonic waveguide. Adapted with permission.[42] Copyright 2011, The Macmillan Publishers Limited.

An extensive research has been conducted in order to increase the SPP propagation length. The basic idea here is to replace the dielectric at the SPP-guiding interface with the lasing medium,[45,49] which can amplify the signal upon stimulated emission into the SPP mode. An essential increase of the propagation length has been demonstrated with free-space optical pumping of quantum dot[50] or dye[51] doped media or semiconductor structures,[52] while all-plasmonic amplification (where the pumping signal is also an SPP wave) has been realized in Er-ion-doped gain medium.[53] As an alternative approach, electric pumping has been proved to be a very efficient and practically feasible approach providing full loss compensation.[54] Ultimately, these efforts led to the demonstration of optically-pumped[55–58] or electrically-pumped[59] plasmonic lasers. Investigation of other amplification-related phenomena, such as exited-state dynamics near the metal surface,[49,60] which defines peculiarity of SPP amplification and modulation speed, and amplified spontaneous emission of SPPs[61] have led to better understanding of the underlying processes.

A complete set of plasmonic circuit elements mimicking traditional dielectric photonic components have been demonstrated, such as bends, splitters, etc. In order to exploit the advantage of signal multiplexing for broadband data transmission, wavelength-selective plasmonic components, such as Mach–Zehnder interferometers (MZIs), waveguide-ring resonators (WRRs) and Bragg gratings have been developed.[7] The functional plasmonic circuitry was further investigated which included active switching components.[62–68] Particularly, an implementation of nanoscale electro-optic effects matching the plasmonic mode confinement has led to the realization of plasmonic switching components of the size of on-chip electronic components.[69] An additional advantage of the plasmonic guiding schemes is the possibility of sending both electric and photonic signals along the same circuitry, thus naturally incorporating electrically-controlled nodes in the plasmonic circuits. In the pursuit of even more ambitious goal of fully-functional all-optical circuitry, plasmonic switching by optical means has been demonstrated on femtosecond time scales.[70] Finally, the realization of SPP sources[71–74] and detectors,[75–77] completes the development of self-contained fully-functional plasmonic circuitry.

1.2. Dielectric-loaded Plasmonic Waveguides and Competing Technologies

One of the important types of the plasmonic waveguides for achieving active functionalities is dielectric-loaded SPP waveguides (DLSPPWs), formed by a dielectric ridge on the metal surface (**Figure 2**). The dielectric results in a higher refractive index for a SPP wave at the metal-dielectric interface compared to that at the metal-air interface, giving rise to SPP modes bound by the dielectric stripe in a way similar to the confinement of guided light modes in conventional optical fibers or planar dielectric waveguides. DLSPP waveguides provide a sought-for trade-off between subwavelength confinement and the propagation loss. High effective index contrast between the mode and the unguided SPP wave at the metal-air interface as well as light in the surrounding space leads to good guiding properties of DLSPPWs. This allows bending and splitting waveguide elements to be just a few micrometers in size at telecommunication wavelengths. The decisive advantage of DLSPPW compared to other SPP waveguide types is that the dielectric ridge can be easily functionalized to provide thermo-optical, electro-optical, or all-optical functionalities, which can be used for the development of active nanophotonic components.[78] Several industry-standard approaches, such as UV photolithography,[79] direct laser writing,[80–82] nanoimprint,[83]
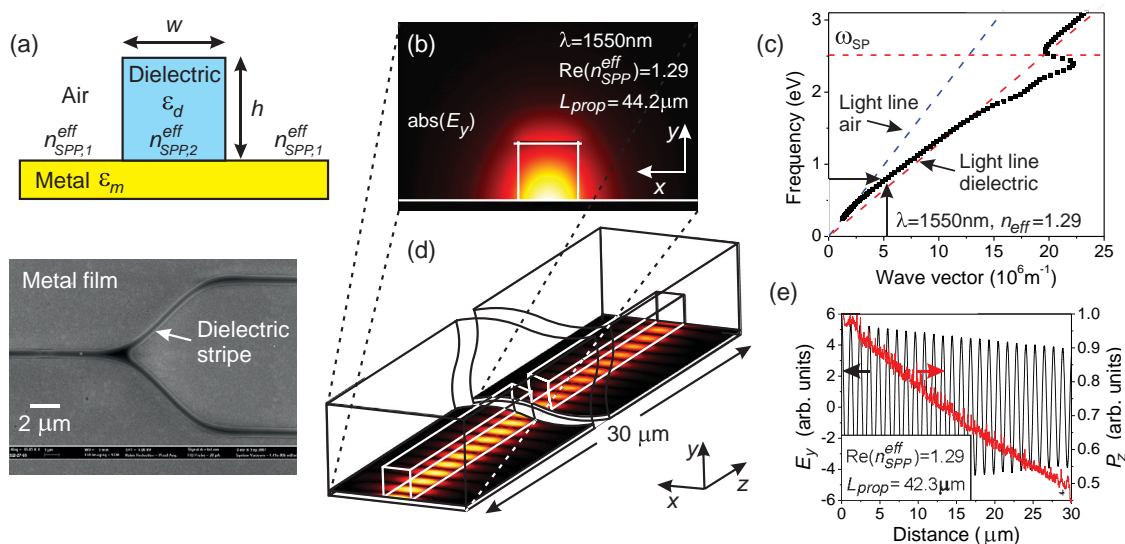

Figure 2. a) Top: cross section of a DLSPP waveguide. Bottom: scanning electron microscopy (SEM) image of the DLSPP waveguide fabricated by deep-UV lithography (top view). b) Abs(E_y) field profile of a fundamental TM$_{00}$ SPP mode in a 600 nm × 600 nm DLSPP waveguide at λ = 1550 nm. c) Dispersion of a TM$_{00}$ SPP mode. d) Simulation setup overlayed with the |E_y| field distribution in a straight DLSPP waveguide. e) Vertical component of the electric field E_y and power flow component P_z along the center of the waveguide at a distance of 10 nm from the metal surface. Adapted with permission.[86] Copyright 2008, the American Physical Society.

Makerials Views

www.MaterialsViews.com

ADVANCED
OPTICAL
MATERIALS
www.advopticalmat.de

REVIEW

or electron-beam lithography[84] can be used for DLSPPW fabrication. Finally, it should be noted that heat dissipation is a very important aspect of the implementation plasmonic waveguides, and here DLSPPWs provide top performance.[85] While, these type of waveguides do not provide highest confinement, they offer the design of enhanced active components with low control powers which can be used within either plasmonic or Si photonic circuitry or indeed integrated with optical fibers.

Si photonic waveguides have sizes comparable with DLSPPW waveguides based on polymers and low propagation loss. In terms of active functionalities, the low propagation loss is essential in Si waveguides in order to harvest small refractive index changes of the mode index induced around the waveguide and influencing primarily the evanescent part of the mode field outside the waveguide. (The latter is in contrast to DLSPPW where it can be induced inside the waveguide just acting at the mode where it has highest intensity.) Thus, the Si photonic components, e.g., MZIs and WRRs should have length sufficient to accumulate significant phase difference of the waveguided mode. This imposes the restrictions on both the minimum size of active components based on Si waveguides as well as the required energies for switching and modulation as, e.g., larger volume should be heated as in the case of thermo-optical modulation. Various Si-waveguide-based modulators and switches have been developed.[87,88] The Si MZI thermo-optical modulators have length ranging from several millimeters down to 60 μm and operate at speeds down to few microseconds and power consumption from tens to hundreds of mW for around 20 dB extinction ratio. In terms of a size × power figure of merit (FOM), this state-of-the-art performance of Si-based active components is inferior to the DLSPPW-based approach.[89,90] Photonic crystal-based designs provide small required powers but have much increased lateral sizes in addition to the optical bandwidth decreased down to few nm.[91,92] The use of fast carrier-injection modulation allows high modulation rates up to tens of Gb s^{-1}, but either at a cost of bigger size (millimeters[93,94] vs. micrometers in the DLSPPW case [95]) or a decreased optical bandwidth (e.g., 0.02 nm for 12 μm ring resonator component,[96] or 18 nm for 80 μm photonic crystal based design[97]).

1.3. Review Outline

In this review, we present the summary of the recent achievements in the development of integrated nanophotonic circuitry based on dielectric-loaded SPP waveguides. Plasmonics-enabled active components can provide smaller size and lower switching energy than traditional nanophotonics components and can be used within Si- or dielectric-based photonic integrated circuitry to reduce energy consumption or indeed in all-plasmonic integration approach on deep-subwavelength scales. In Section 2, the principles of confinement and guiding photonic signals in a form of plasmonic waves in highly-integrated photonic circuitry will be discussed and a general concept of dielectric-loaded plasmonic waveguides will be introduced. Sections 3, 4, and 5 will overview passive, wavelength-selective and active DLSPPW components of various designs, respectively. Section 6 will benchmark the guiding performance of DLSPPWs against that

of other plasmonic waveguides. Approaches for signal amplification in DLSPP waveguides will be introduced in Section 7. Finally, Section 8 will be devoted to the discussion of other plasmonic waveguide designs based on the DLSPPW principle and applications of DLSPPWs beyond integrated nanophotonics.

2. Optical Signal Guiding in DLSPP Waveguides

2.1. Guiding Principle and Modal Properties

Plasmonic mode guiding along a DLSPPW is based on a principle of refractive index contrast. A plasmonic wave propagating at a metal–dielectric interface has a wave vector

$$k_{SPP} = \frac{2\pi}{\lambda} \sqrt{\frac{\varepsilon_d \varepsilon_m}{\varepsilon_d + \varepsilon_m}} \qquad (1)$$

defined by the permittivities of metal ε_m and dielectric ε_d, and the wavelength of light λ. Due to the inherent losses, dielectric constant of metal possesses an imaginary part and, consequently, the wave vector of the SPP wave has a complex value. Its real part defines the effective index of the mode

$$n_{SPP}^{eff} = \frac{\lambda}{2\pi} \mathrm{Re}\left(k_{SPP}\right) = \mathrm{Re}\left(\sqrt{\frac{\varepsilon_d \varepsilon_m}{\varepsilon_d + \varepsilon_m}}\right) \qquad (2)$$

while the imaginary part determines its propagation length (distance at which the intensity of the mode decrease in e times):

$$L_{SPP}^{prop} = \frac{1}{2\mathrm{Im}\left(k_{SPP}\right)} = \frac{\lambda}{4\pi \mathrm{Im}\left(\sqrt{\frac{\varepsilon_d \varepsilon_m}{\varepsilon_d + \varepsilon_m}}\right)} \qquad (3)$$

In the case of the DLSPP waveguide, it follows that the effective index in the ridge region will be larger than that in the regions to the right and to the left of the ridge (Figure 2a) $n_{SPP,2}^{eff} > n_{SPP,1}^{eff}$. Thus, in analogy to the optical fiber and planar dielectric waveguide geometries, a plasmonic guided mode supported by DLSPPW will be formed. The propagation length in DLSPPW depends on the proportion of the mode energy located in the metal and can be calculated using approximate methods or rigorous numerical simulations, as will be discussed below.

We initially consider an Au-based plasmonic waveguide with a low-index, polymer-defined dielectric ridge. Using approach based on effective-index method,[98] general rules and trade-offs relevant to the DLSPPW design can be revealed (**Figure 3**). At the first step, considering 4-layer guiding structure at the telecommunication wavelength of 1550 nm (Figure 3b), the propagation length of the SPP wave was found to have a non-monotonous behavior as the thickness of the ridge-polymer layer is changed (Figure 3c). For all the modes supported by the structure, the propagation length initially decreases with the decrease of the polymer thickness below the value of 1 μm due to the fact that the electromagnetic field is efficiently pushed into the metal and experiences higher losses. However, for much thinner dielectric layers, e.g., 200 nm for
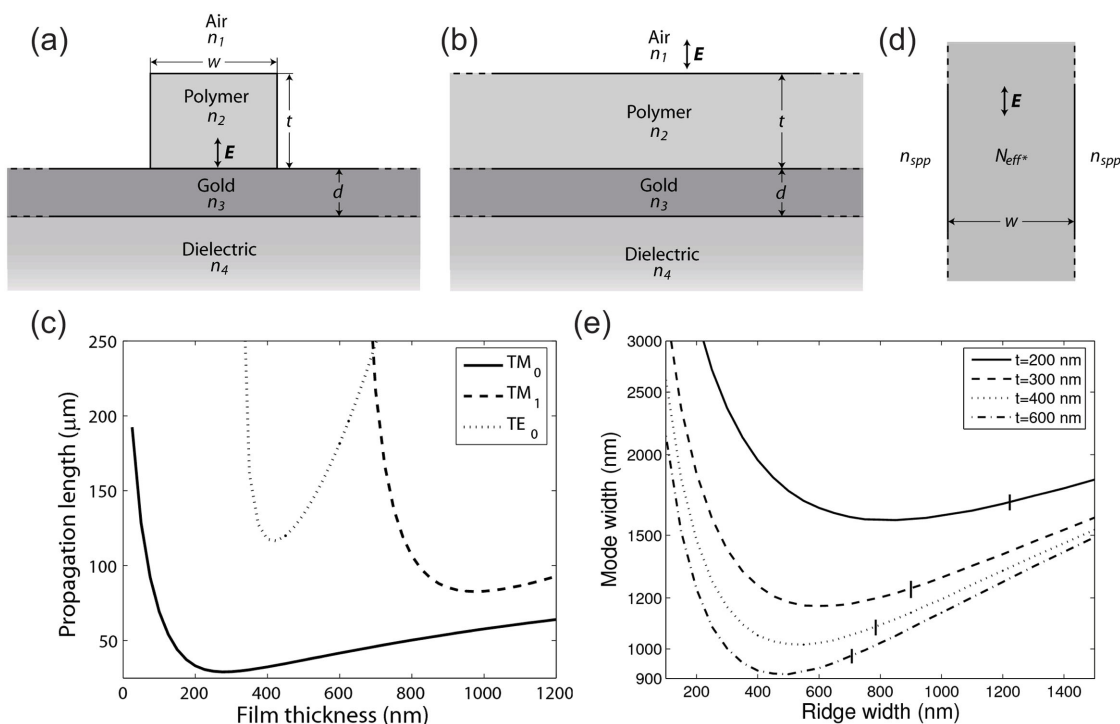
ADVANCED
OPTICAL
MATERIALS
www.advopticalmat.de

Materials Views
www.MaterialsViews.com

REVIEW

Figure 3. a) Cross-sectional view of the DLSPP waveguide operating at $\lambda = 1550$ nm formed by a rectangular polymer ridge ($n_2 = 1.535$) on a gold film ($n_3 = 0.55 - 11.5i$) deposited onto a substrate with $n_3 = 1.6$ and surrounded by air $n_1 = 1$. b) The four-layer and c) three-layer structures considered in the first and the second steps of the effective-index simulations, respectively. d) Characteristics of modes supported by the four-layer structure presented in (b) and analyzed in the first step. e) The mode width (logarithmic scale) dependence on the ridge width for four different values of the ridge thickness t. The vertical lines mark the end of the single-mode regime. Reproduced with permission.[98] Copyright 2007, The American Physical Society.

TM_0 mode relevant to the formation of the fundamental TM_{00} DLSPP mode (Figure 2b,d,e), the propagation length starts to increase and becomes very similar to the SPP mode at an Au–Air interface.

Using the effective indexes of the 4-layer structure (Figure 3d), it was found that there is an optimal ridge width 500 to 800 nm, corresponding to the minimal lateral size of the DLSPPW mode (Figure 3e). At ridge widths larger than the optimal, the DLSPPW mode will occupy all the available space from one edge to another, corresponding to larger lateral mode sizes, whereas at ridge widths smaller then the optimal the SPP fields will be laterally pushed outside the ridge, leading again to poorer confinement. In addition to strong lateral confinement and low propagation loss, single-mode guiding by the plasmonic waveguide structures is usually desired in order to avoid various mode dispersion and interference effects. Accordingly, the condition for single mode guiding for the considered example is the waveguide thickness smaller than 600 nm and the waveguide width smaller than 650 nm, which corresponds to the waveguide size of approximately $\lambda/2.5 \times \lambda/2.5$ in terms of the operational wavelength.

The results of the effective-index modal analysis were compared with the rigorous finite-element simulations, and good agreement between the two methods was demonstrated.[98] The height and the width of the waveguide were optimized, defining figures of merit to describe the suitability of a given configuration to a particular application requiring either the longer propagation length or stronger confinement.[99–103] Other shapes of the

dielectric ridge, such as the one produced by a nanofiber,[104,105] semi-elliptical,[106] or non-ideal ridge shapes formed in the actual fabrication process,[103] have been investigated, considering the influence of the waveguide geometry on the DLSPPW performance. The implementation of high-dielectric index material, such as Si or InGaAs, allows to reduce the width of the waveguide down to 200 nm × 200 nm (or approximately $\lambda/8 \times \lambda/8$), but for the price of active functionalities provided by a doped polymer. High-dielectric index materials and other plasmonic metals will be considered in details in Section 8.

Comprehensive numerical analysis of the guiding properties of DLSPP waveguides considered a polymer stripe waveguide with a rectangular cross section of 600 nm × 600 nm deposited onto a gold surface (Figure 2a).[86] At wavelengths above ≈1250 nm, the waveguide is singlemode for SPP waves, supporting only a fundamental TM_{00} plasmonic mode. The mode is highly localized in the dielectric core of the waveguide at the metal–dielectric interface (Figure 2b,d,e). At low frequencies (Figure 2c), large amount of energy of the mode is located in the air region, and, therefore, the mode dispersion is close to the SPP dispersion at the metal–air interface. At higher frequencies, the mode energy is mostly localized inside the dielectric; consequently, the mode dispersion follows the SPP dispersion at the metal–dielectric interface. The dispersion curve experiences back-bending and crosses the light line due to the increased, frequency-dependent Ohmic losses in Au. For the signal wavelength $\lambda = 1550$ nm, the chosen geometrical parameters of the waveguide provide the optimum ratio between mode

www.MaterialsViews.com

ADVANCED
OPTICAL
MATERIALS
www.advopticalmat.de

REVIEW

confinement and attenuation.[98] The SPP mode propagates along the waveguide, keeping its field profile constant and its energy exponentially decays with distance due to the Ohmic losses in the metal. The mode characteristics were estimated from a complex value of its effective index, which gives Re(n_{eff}) = 1.29 and L_{prop} = 44.2 μm for the polymer refractive index of 1.5. The high mode effective index ensures strong guiding characteristics leading to a small size of DLSPPW components, while relatively large L_{prop} gives the opportunity for the realization of elaborated circuitry network within the available attenuation length.

After initial observations of multimode DLSPP waveguiding,[107] the first experimental studies of single-mode polymer-based waveguides were performed, revealing essentially the same guiding characteristics as predicted by theory.[108] The waveguides, fabricated using UV photolithography, were used with a funnel facilitating coupling of the excited broad SPP wavefront into the single mode waveguide. The optical characterization of the guided plasmonic modes was performed using scanning near-field microscopy (SNOM). The propagation length of the mode was observed to become gradually larger with the increase of the operational wavelength at the price of poorer mode confinement and lower mode effective index (Figure 4), confirming the theoretical predictions. It was found, however, that the measured propagation lengths, being in a qualitative agreement, were longer than those expected from the EIM calculations (Figure 4g). This most likely was due to the difference in the optical properties of the gold used in calculations and that in the experiment (gold permittivity is known to be essentially influenced by the deposition method employed). The intensity oscillation patterns (e.g., the one particularly pronounced in Figure 4f) are due to the interference of the DLSPPW mode with Re(n_{eff}) = 1.21 with its reflection from the waveguide termination.

2.2. Integration Level and Data Transfer Characteristics of a DLSPPW

The key question in practical applications of SPP guiding approach is the level of ultimate photonic integration of a circuitry built on its basis. It is determined by a cross-talk between two parallel DLSPP waveguides placed at some distance from each other (Figure 5a) leading to the signal mixing between the waveguides.[109] If the SPP mode is initially launched in one of the waveguides (bottom in Figure 5a field map), during the propagation its energy is gradually transferred into the neighboring waveguide due to the overlap of the waveguides' modes. As a consequence, the mode starts to oscillate between the waveguides with a gradually decreasing amplitude due to the Ohmic losses (Figure 5a). Clear beating of the DLSPPW mode between coupled waveguides was experimentally observed using the leakage radiation microscopy (Figure 5b).[110,111] The strength of coupling between the waveguides is represented by a coupling length L_c, the distance along the waveguide at which the energy of the propagating mode is fully transferred to the neighboring one. The increase of the coupling length with the distance between the waveguides has an exponential dependence (Figure 5c).[109,112] When the waveguides are close to each other (e.g., d = 700 nm, so that the distance between the waveguide edges is 100 nm), the tunneling between the waveguides is very efficient with L_c = 4.6 μm. Making use of this strong coupling regime at smaller separations, waveguide couplers and splitters as well as wavelength-selective components in a form of directional couplers, were realized (Sections 3.3 and 4.3). In the other extreme case, when the cores of the waveguides are significantly separated (e.g., d = 2.6 μm), the coupling between the waveguides is extremely weak (L_c = 2.3 mm), so at this distance the waveguides are practically not coupled. Using as a criterion that less than 15% of signal cross-talk is
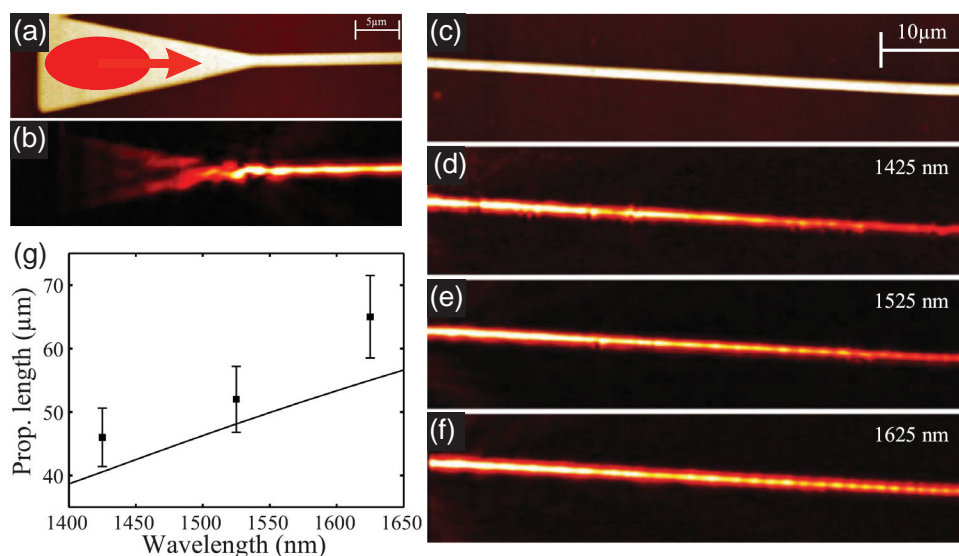

Figure 4. a) Topography with an indicated illumination spot and b) SNOM images (at λ = 1550 nm) of a taper coupling component, adiabatically funneling plasmonic waves into a straight DLSPP waveguide. c) Topography and d–f) near-field optical images of a straight waveguide at different free-space excitation wavelengths: d) λ = 1425 nm with L_{prop} = 46 μm, e) λ = 1525 nm with L_{prop} = 52 μm, and f) λ = 1625 nm with L_{prop} = 65 μm. g) Experimental (points) and theoretical (line) dependences of the propagation length on the operational wavelength. Adapted with permission.[108] Copyright 2008, the American Physical Society.
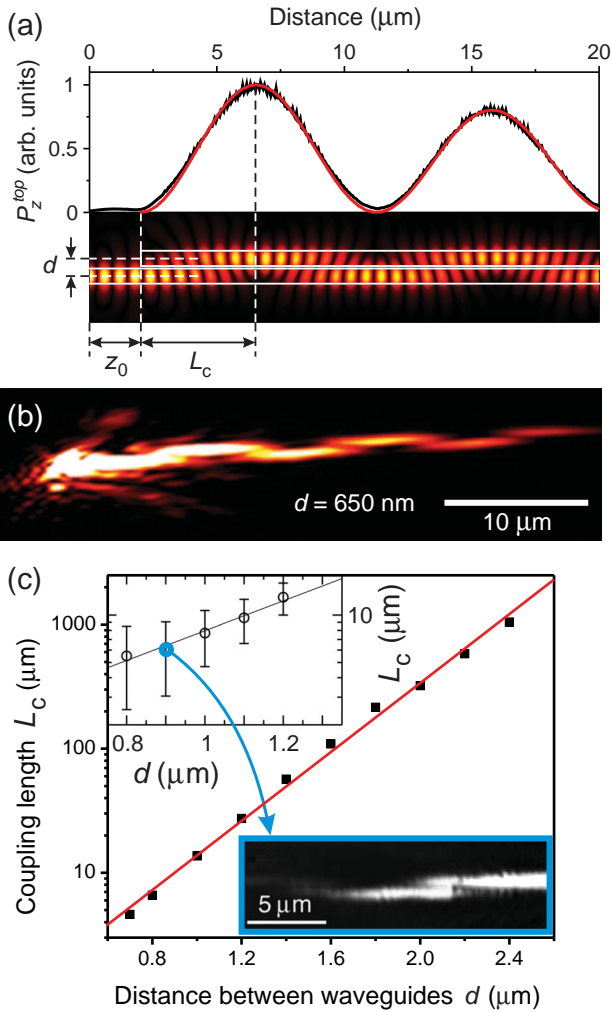
Figure 5. a) Coupling between two parallel 600 nm × 600 nm PMMA-based DLSPP waveguides at λ = 1550 nm. Adapted with permission.[86] Copyright 2008, the American Physical Society. b) LRM image of a cross-talk between two parallel 550 nm (w) × 100 nm (h) PMMA-based DLSPPW waveguides at λ = 633 nm. Adapted with permission.[110] Copyright 2010, American Institute of Physics. c) Dependence of the coupling length L_c on the distance between the waveguide centers d for λ = 1550 nm. Adapted with permission.[109] Copyright 2007, American Institute of Physics. Insets: (top) experimentally measured dependence of the coupling between 700 nm (w) × 60 nm (h) SiO$_2$ DLSPPW waveguides at λ = 800 nm as a function of center-to-center distance between them; (bottom) LRM image of the coupling process for d = 0.9 μm. Reproduced with permission.[112] Copyright 2007, American Institute of Physics.

allowed during the propagation in neighboring waveguides over the distance of L_{prop}, the single mode DLSPPW operating at the telecom wavelength provide the integration level of $d \approx 1.9$ μm, corresponding to $\approx 1.2\lambda$. The other characteristic defining the integration level of the photonic circuitry, such as the achievable size of the circuit components as well as their performance will be discussed below in Sections 3 and 6.

A crucial parameter defining the performance of the waveguide is the data bit-rate it can support. For a single-mode waveguide, if nonlinearities are neglected, it is determined by the frequency dispersion of the waveguide modes, which leads to

different propagation characteristics for spectral components within signal carrying pulses, broadening them as they propagate in the waveguide.[113] The maximum bandwidth in a single data stream for a waveguide of a given length is then determined by the highest rate of the pulses, at which they can still be distinguished as separate at the output. In the case of lossy waveguides, the spreading of the pulses depends on the second order dispersion of both real and imaginary parts of the propagation constant β:[113]

$$B \sim L^{-1/2} \left(\left(\frac{\partial^2 \text{Re}\{\beta\}}{\partial \omega^2} \right)^2 + \left(\frac{\partial^2 \text{Im}\{\beta\}}{\partial \omega^2} \right)^2 \right)^{-1/4} \tag{4}$$

For DLSPPWs and other plasmonic waveguides compared in this review (see Section 6), it was found that $\left(\partial^2 \text{Im}\{\beta\} / \partial \omega^2 \right) \ll \left(\partial^2 \text{Re}\{\beta\} / \partial \omega^2 \right)^2$, and the bandwidth can be estimated as as[54]

$$B = \sqrt{\frac{1}{8\pi} \frac{1}{L} \frac{1}{\frac{\partial^2 \text{Re}\{\beta\}}{\partial \omega^2}}} = \sqrt{\frac{1}{8\pi} \frac{1}{L} \frac{\upsilon_g^2}{\frac{\partial \upsilon_g}{\partial \omega}}} \tag{5}$$

where υ_g is the group velocity of the mode, β is its propagation constant, and L is the waveguide length. The bandwidth depends on the waveguide parameters, its geometry and material. Taking a characteristic length of DLSPPW interconnect to be $L = L_{prop}$, the theoretical limit for the bandwidth can be estimated (**Table 1**). Varying waveguide's height and width in the region 400–600 nm (lower values will give an effective mode index below 1.1, resulting in much worse guiding characteristics, while values higher than 600 nm results in multimode guiding), it was found that a poly-methyl-methacrylate (PMMA) based 600 nm × 600 nm waveguide has the highest bandwidth. Generally, the dispersion-defined DLSPP-based interconnect bandwidth B reaches very high values of tens of Tb s^{-1}. The practical bandwidth will be defined in this case by the nonlinearities of metal and dielectric, the bandwidth of available modulators and detectors, and multiplexing methods.

Experimentally, the bandwidth of 10 Gb s^{-1} in a single data stream has been directly experimentally measured for DLSPP waveguides (PMMA/Au, 500 nm × 600 nm), with error-free operation and no visible distortion to the eye diagram in comparison with the reference measurements (**Figure 6**).[114] Further improvements was obtained with the

Table 1. Theoretical limit for bandwidth of PMMA- or Si-on-gold DLSPP waveguides of various designs (width × height, core material), estimated at a wavelength of 1550 nm.

Design	B [Tb s^{-1}]
600 nm × 600 nm, PMMA	39
600 nm × 400 nm, PMMA	23
400 nm × 600 nm, PMMA	23
400 nm × 400 nm, PMMA	17
200 nm × 200 nm, Si	39

www.MaterialsViews.com

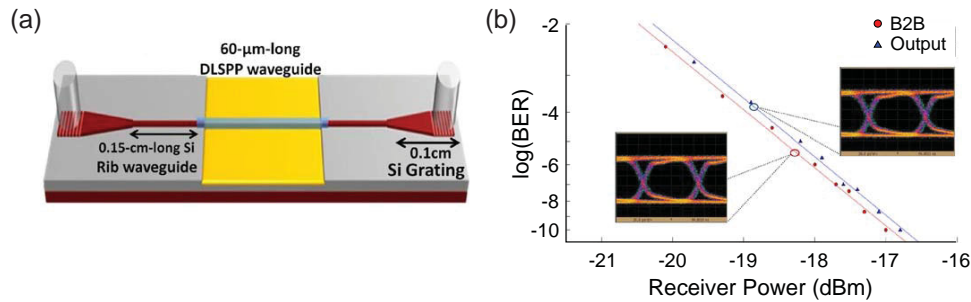ADVANCED
OPTICAL
MATERIALS
www.advopticalmat.de

REVIEW

Figure 6. a) Experimental setup used for the 10 Gb s^{-1} transmission through a straight DLSPP waveguide at telecommunication wavelengths. b) Bit error rate measurements and eye diagrams of the output signal transmitted though a 60-µm Si-DLSPP waveguide and the reference signal (B2B, same path without the DLSPPW section). Reproduced with permission. Copyright 2012, G. Giannoulis.

demonstration of 40 Gb/s data transmission rate in a single data stream and implementation of the WDM technique by sending multiple data streams at different wavelengths.[115] This yielded the multiplexed 12 × 40 Gb s^{-1} = 480 Gb s^{-1} total data bit-rate experimentally demonstrated in a single DLSPP waveguide.

3. DLSPPW Passive Components

In this section we will discuss various aspects of routing plasmonic signals in DLSPPW circuitry. Starting with an overview of diverse methods for DLSPPW mode excitation, we will continue with interfacing the DLSPPW circuitry with conventional photonic waveguides, and then discuss the designs and performance of various DLSPPW passive components, such as bends, splitters, ring resonators, and others.

3.1. Excitation and Detection of DLSPPW Modes

From a practical point of view, coupling of light to DLSPPW modes can be achieved by focusing the laser beam at the end of a DLSPP waveguide.[110] Upon diffraction at the edge of the dielectric ridge, the necessary component can be supplied to the wave vector of the incident light to provide matching to the wave vector of the DLSPPW mode, albeit with low efficiency (**Figure 7**a). To achieve better coupling efficiency to the DLSPPW modes, two standard approaches to SPP mode excitation were successfully implemented: 1) based on total internal reflection and 2) grating-assisted coupling. In the first method, a plane SPP wave was excited using the Kretschmann–Raether configuration either in front of a funneling structure produced by gradual widening of the waveguide or directly inside it[108,116] (the latter scheme greatly reduces background scattering signal). During propagation towards the narrow end of the
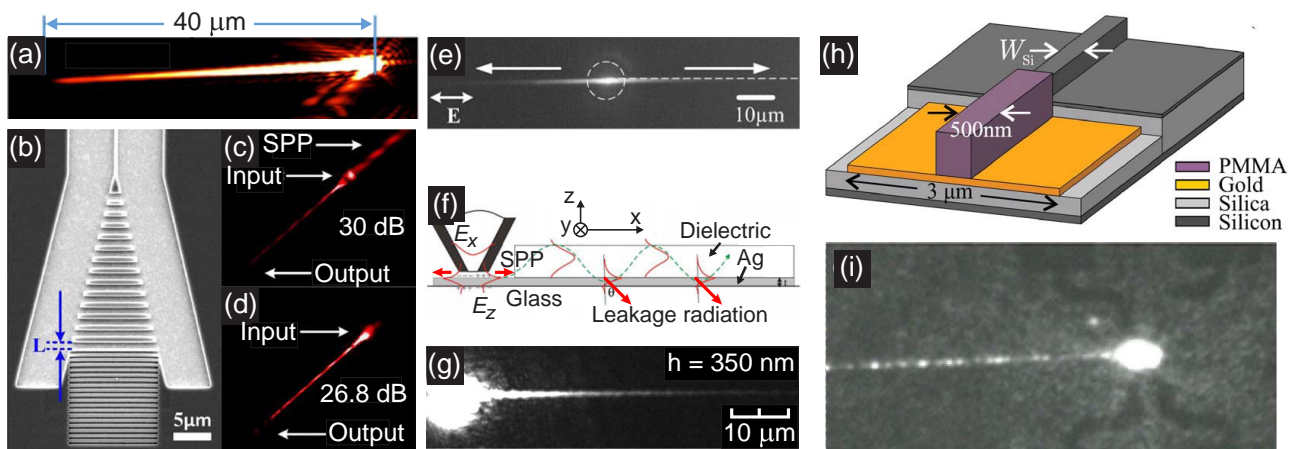

Figure 7. a) Leakage radiation microscopy (LRM) image of a DLSPPW mode launched by focusing of a λ = 633 nm laser beam at the edge of the waveguide. Reproduced with permission.[110] Copyright 2010, American Institute of Physics. b) SEM-image of the funnel with an incorporated coupling grating and a Bragg reflector grating to maximize the coupling efficiency. c,d) LRM images of the DLSPPW mode launched at telecommunication wavelength using the coupler presented in (b) with non-optimised (c) and optimised (d) Bragg gratings. Reproduced with permission.[117] Copyright 2012, IEEE. e) LMR image of fluorescence coupled to the DLSPPW mode. Reproduced with permission.[118] Copyright 2010, Optical Society of America. f) Schematic and g) LRM image of DLSPPW mode launched using a tapered fiber. Reproduced with permission.[119] Copyright 2011, Springer. The low propagation length of the DLSPPW mode in (e) and (g) is due to the use of visible wavelengths (576 and 650 nm, respectively) at which the losses in metal are high. h) Schematic of the end-fire interfacing of a SOI photonic waveguide with a DLSPPW. i) Interfacing a Si wire waveguide (visible as a horizontal bright trace at the left-hand side) with the DLSPPW at λ = 1550 nm, the bright spot marks the position of DLSPPW; an output Si waveguide (not visible due to attenuation of the mode in the DLSPPW section) is to the right of the DLSPPW. Reproduced with permission.[120] Copyright 2012, IEEE.

REVIEW

funnel, the SPP wave is adiabatically confined to the waveguide and coupled to a well defined DLSPPW mode (Figure 4a,b). Since for the SPP wave interacting with the taper boundaries the total internal reflection conditions are satisfied, there is no leakage of the SPP waves outside the taper and high coupling efficiency can be achieved. The absence of the coupled mode beating inside the waveguide confirms that the designed DLSPPW structure indeed only supports a single plasmonic mode.

Another typical coupling approach is based on diffraction grating structures, which in the case of SPP excitation on a planar surface were experimentally shown to provide a ≈45% coupling efficiency.[121] Combining this method with the tapering structure, an efficient grating coupler to the sub-wavelength DLSPPW mode was developed (Figure 7b–d).[117] The grating was realized in a form of periodic array of polymer ridges, which allows its fabrication together with the DLSPP waveguide in a simple one-step lithography process. By optimizing geometrical parameters of the grating, the coupling efficiencies up to 20% were demonstrated. To achieve coupling directionality from the symmetric grating, the Bragg grating (having potential reflectivity up to 85% [122]) was introduced to prohibit SPP excitation in the direction opposite to the waveguide (Figure 7b). The parameters of the reflector and the gap between the two gratings need to ensure that generated (in the waveguide direction) and the reflected (from the Bragg grating) SPP waves are in phase (Figures 7c,d). The relatively low insertion loss of such couplers (down to 25 dB), low dispersion and loss below 35 dB in a wavelength range of 1525–1575 nm make these coupling components suitable for telecommunication applications. As a variation of this method, a semi-circular grating coupler design which additionally provides focusing of the launched SPP wave into the DLSPP waveguide was also numerically investigated.[123]

An interesting DLSPPW mode excitation method is based on the generation of SPPs directly in the waveguide doped with fluorescent centers by optical pumping. If an emitter (atom, quantum dot, dye molecule, etc.) is located in the vicinity of a metal surface (typically from tens to few hundreds of nanometers), it can spontaneously emit directly into the SPP mode.[60] This process was used for generation of the plasmonic signal in the PMMA DLSPP waveguides doped with Rhodamine B molecules (Figure 7e).[118] The SPP mode is excited and propagates along the DLSPP waveguide in both directions from the excitation spot. The wave vector of the mode was found to be $1.103k_0$ ($k_0 = 2\pi/\lambda$, $\lambda = 576$ μm) which confirms that the excited mode is the fundamental TM_{00} mode of the DLSPP waveguide with a width of 160 nm and a height of 68 nm.

For practical applications, interfacing of DLSPPW circuitry with the standard external optical networks has a particular importance. Several methods have been developed for coupling DLSPP waveguides to conventional optical fibres[124] and silicon-on-insulator (SOI) ridge waveguides.[125,120] The basic approach implemented here is the end-fire coupling when the fiber or a waveguide is positioned in line with the DLSPPW waveguide in the near-field proximity to its edge. To achieve a better overlap between the fiber and waveguide modes, the DLSPPW is usually gradually widened towards the fibre edge. The excited SPP mode is then funneled into the waveguide in

the same manner as discussed previously. One can also use the diffraction grating based couplers to interface optical fibres, similar to described above (Figure 7f,g).[119]

A typical scheme for interfacing the DLSPP and SOI waveguides is shown in Figure 7h. The particularly good coupling was achieved for PMMA-coated SOI waveguides, when the DLSPPW ridge material seamlessly transforms into the SOI ridge waveguide coating (not shown in the figure), which automatically insures a good interface quality. The coupling efficiency in this case was experimentally shown to reach almost 80% for both in-coupling (SOI-to-DLSPPW) and out-coupling (DLSPPW-to-SOI) scenarios.[125] The coupling between uncoated SOI ridge waveguides and DLSPPWs was further extended to more compact Si-wire waveguides, when a silicon film in the SOI ridge waveguide is removed (Figure 7h,i).[120] Upon optimization of the coupler geometrical parameters (Si-waveguide width and vertical offset), the coupling efficiency can be increased to ≈85%. The experimentally measured coupling efficiencies for an uncoated SOI ridge waveguide to a DLSPPW was slightly lower due to imperfection of the facets, slight waveguide misalignment as well as a gap between the gold film and the silicon waveguide edge, but still approaching high values ranging from 35 to 60%, depending on the particular sample.

An integrated detector of the plasmonic signal completes the design of a DLSPPW-based interconnect (**Figure 8**).[126] To implement it, a nanoscale slit was placed beneath the DLSPP waveguide in the gold film, while the whole structure was fabricated on a Si substrate. When the DLSPPW mode reaches the slit,
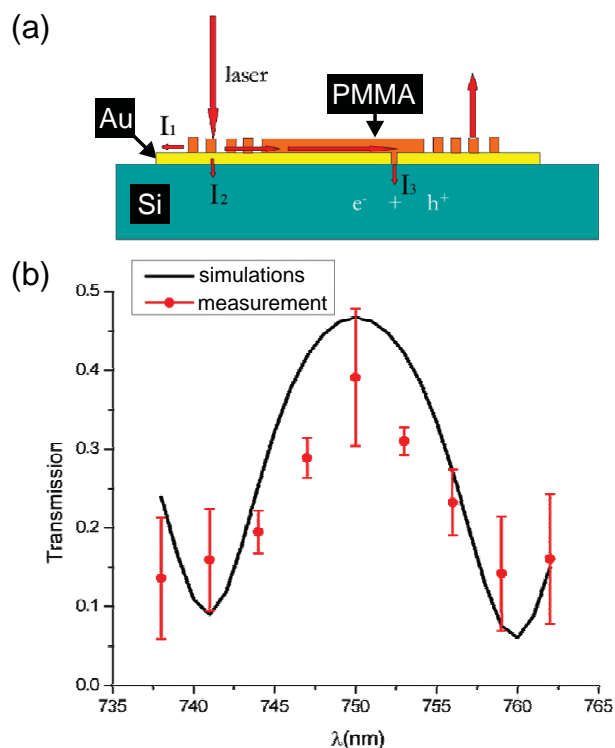

Figure 8. a) Principle of integrated electric detection of a DLSPPW mode. b) Transmission spectrum of the DLSPPW ring resonator measured with the detection scheme presented in (a). Reproduced with permission.[126] Copyright 2014, American Chemical Society.

www.MaterialsViews.com

ADVANCED
OPTICAL
MATERIALS
www.advopticalmat.de

REVIEW

it is partly coupled to a gap SPP mode in the slit. The intense electromagnetic field of the mode produces hot electrons with kinetic energies exceeding the height of the Schottky barrier at the boundary of the metal and the semiconductor substrate. The hot carriers generate electron-hole pairs in silicon, which under applied voltage result in a photocurrent. Thus, a monolithic integration of a detector with DLSPPW circuitry can be implemented.

3.2. Waveguide Bends

A basic component required to build photonic circuitry is a waveguide bend. A 90° waveguide bend can be implemented using a waveguide section of a circular shape with a radius r (**Figure 9**).[86,112] The calculated near-field distributions show that during propagation along the curved section, the SPP guided mode experiences radiation losses in a form of free-space light and SPP waves on the surface outside the guide. The dependence of transmission $T_b = I_{b1}/I_{b0}$ through the bend T on the radius of the bend r (Figure 9a, curve (i)) is determined by a trade-off between two sources of losses. For small bend radii (sharp bends), radiation losses play a dominant role due to more efficient coupling to light and unguided SPPs at the surrounding metal surface.[127] For large radii, where the radiation losses are small, the absorption Ohmic losses become dominant due to the increase in the length of the bend section. At the optimal value of the bend radius $r \approx 5$ μm, when the total losses in the bend are minimal, the transmission is as high as 75% (corresponding to signal loss of 1.3 dB) at a telecom wavelength of 1550 nm. Moreover, if the losses in metal are compensated by, e.g., gain (Section 7), the transmission can be above 95% (Figure 9a, curve (ii)). The obtained bend radius ultimately defines small size of DLSPPW components, such as splitters, waveguide ring resonators, etc.

A comprehensive experimental investigation of bend loss of single-mode DLSPPW was performed using S-bends, i.e., double-bends, connecting two parallel waveguides with an offset with respect to each other (**Figure 10**a).[116] The design of S-bends was based on sine curves, ensuring continuous bend curvature and, therefore, adiabatic evolution of the DLSPPW mode throughout the bend. The bends with small offsets ($d \leq 5$ μm) show an excellent performance with the transmission up to 70% (Figure 10b), which gradually decreases with the offset increase due to the radiation and absorption losses (Figure 10c). At the same time, even the S-bend with the largest offset ($d = 15$ μm), corresponding to the smallest curvature radius of 1.95 μm, transmits a substantial signal (Figure 10d), confirming robust guiding properties of DLSPPWs. The experimental and theoretical transmission values were found in good agreement with each other (Figure 10e). The striking agreement was also observed in the field maps comparing the intensity distributions from the simulations with the near-field images obtained in the experiment (c.f. Figures 10b,d and insets in Figure 10e). The transmission shown in Figure 10e reflects not only the radiation losses due to the waveguide curvature, but also the DLSPPW mode propagation loss due to absorption in gold, accumulated over 10-μm-long (in the horizontal direction) S-bends. With the known DLSPPW propagation length ($L_{prop} \approx 50$ μm), it was possible to separate the contributions of the loss channels. For $d \leq 3$ μm the bend radiation loss was found to be less than 10%, whereas for $d > 6$ μm it constitutes the main loss contribution. The numerical study of how the S-bend transmission depends on the S-bend shape and length, keeping the same offset between the waveguides shows that among various shapes of the S-bend, the shape defined by the sine curve provided the best performance.[86]

3.3. Waveguide Splitters

The performance of DLSPPW Y-splitters at telecommunication wavelengths was extensively studied using scanning near-field optical microscopy in conjunction with FEM numerical simulations.[116] The splitters with different arm separations ranging from 3 to 30 μm were fabricated using deep-UV lithography, keeping the splitter horizontal length constant (**Figure 11**a,b). The Y-splitters have a pronounced rounding of the junction area with ≈300 nm radius (inset in Figure 11), due to limited
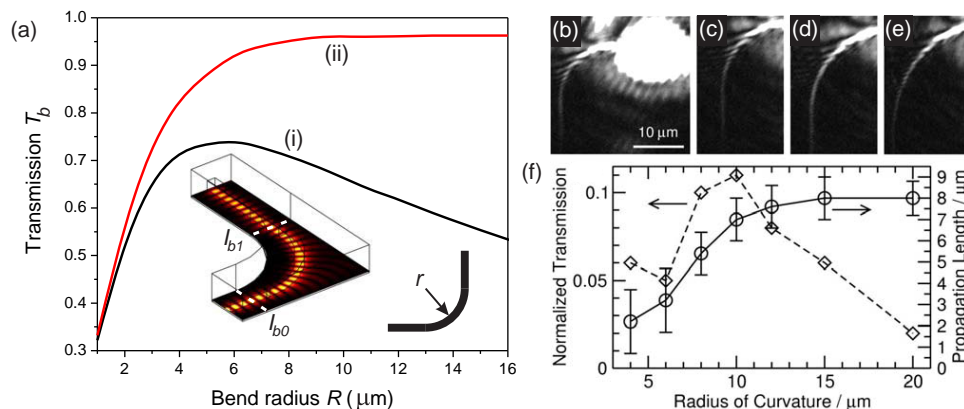

Figure 9. a) Transmission of a 90° circular waveguide bend as a function of its radius r for PMMA-based waveguide with a cross-section of 600 nm × 600 nm at $\lambda = 1550$ nm. Curve (i) corresponds to dielectric with $\varepsilon_{polym} = 2.36$ and curve (ii) corresponds to dielectric with an optical gain with $\varepsilon_{polym} = 2.36 -0.00944i$. Adapted with permission.[86] Copyright 2008, American Physical Society. b–e) LRM images at $\lambda = 800$ nm of waveguide bends with bend radii of b) 10, c) 12, d) 15, and e) 20 μm. f) The dependence of the bend transmission derived from (b–e) on the bend radius. Reproduced with permission.[112] Copyright 2007, American Institute of Physics.
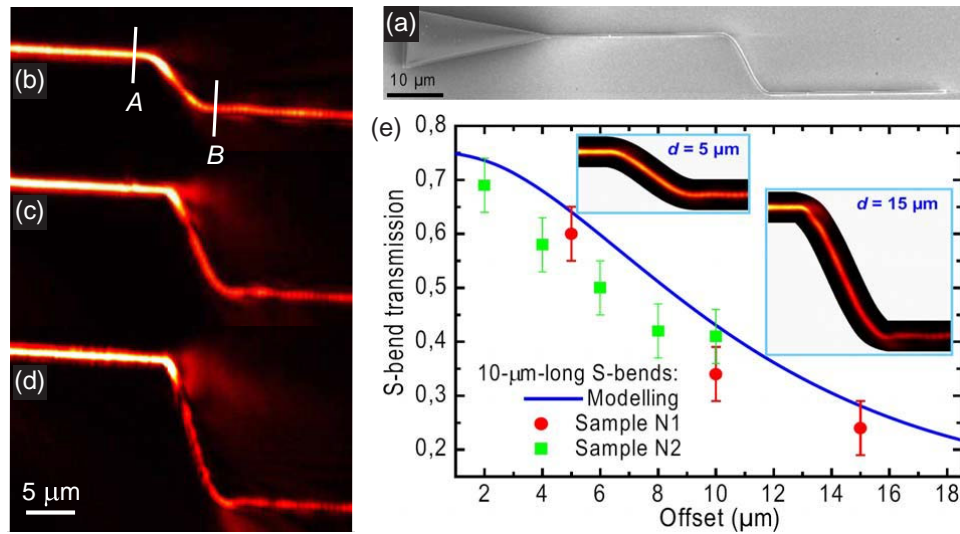
ADVANCED
OPTICAL
MATERIALS

www.advopticalmat.de

Materials
Views
www.MaterialsViews.com

REVIEW

Figure 10. a) SEM image of a tapered waveguide structure comprising a 10 μm long S-bend with an offset of 10 μm. b–d) Near-field optical images of the SPP mode propagation in a 10 μm long S-bend with an offset of b) 5 μm, c) 10 μm, d) 15 μm at $\lambda = 1550$ nm. e) S-bend transmission dependence on the offset distance between the arms for the 10 μm long (in the horizontal direction) S-bends determined from the SNOM images and by numerical modeling. Insets show simulated intensity distributions in two S-bends with different offsets that should be compared to the optical images shown in (b) and (d). Adapted with permission.[116] Copyright 2008, American Optical Society.

resolution of the fabrication technique. Such a rounding prevents adiabatic transformation of the input mode into the outgoing modes in the waveguide branches, resulting, therefore, in a radiation loss mostly into SPPs propagating on a metal surface in the area between the branches (Figure 11c,d). The Y-splitters with a 300 nm radius rounding of the junction area show an ≈20% decrease in transmission, compared to the adiabatic splitters, which is in good agreement with the experimental results. The resolution in the DLSPPW fabrication and consequently

the performance of the splitters can be improved, e.g., by exploiting optical proximity correction techniques. The total transmission can be further increased up to ≈95% for the 10 μm long splitter by introducing amplification to reduce absorption losses (see Section 7). Even without amplification, with the arm separation of 2.6 μm, the splitter length can be reduced to about 6 μm without a practical decrease of the splitter performance, providing a total signal in the output of ≈75%.[86] It was also demonstrated that by breaking the symmetry of the splitter
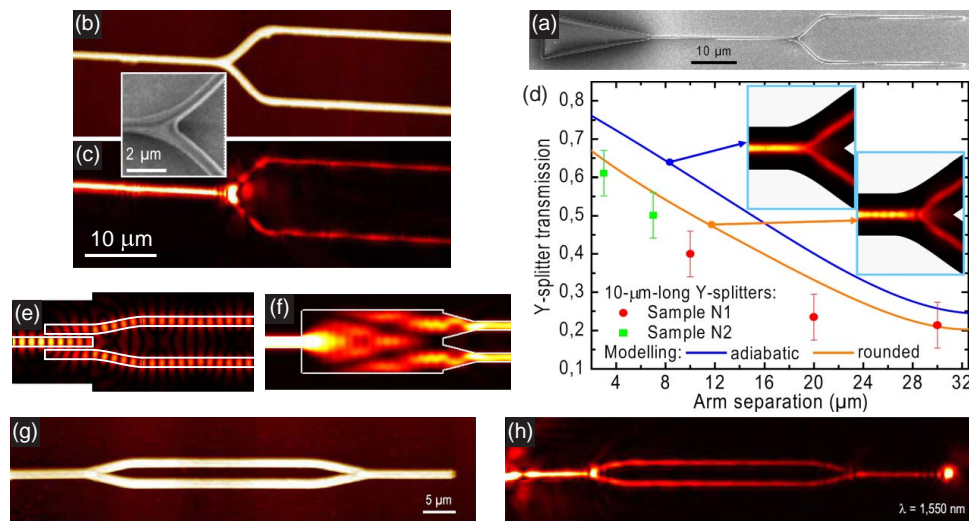

Figure 11. a) SEM image of a Y-splitter with an arm separation of 10 μm. b) Topography and c) near-field optical images at $\lambda = 1550$ nm of the Y-splitter shown in (a) along with an inset showing an SEM image of the junction area. d) Experimental and simulated dependeneces of Y-splitter transmission on the arm separation. Insets show the simulated intensity distributions in the Y-splitters with adiabatic arm separation and a 300 nm radius rounding of the junction area (the latter should be compared to the optical image in (c)). All the splitters are 10 μm long in the horizontal direction. Adapted with permission.[116] Copyright 2008, Optical Society of America. SPP mode propagation in a splitter based on e) coupled DLSPP waveguides (adapted with permission,[86] Copyright 2008, American Physical Society) and f) multimode interference (reproduced with permission.[128] Copyright 2009, Optical Society of America) at $\lambda = 1550$ nm. g) Topography and h) near-field optical images at $\lambda = 1550$ nm of a Mach–Zehnder interferometer with an arm separation of 3 μm. The SPP mode propagates from left to right. Adapted with permission.[116] Copyright 2008, Optical Society of America.

www.MaterialsViews.com

ADVANCED
OPTICAL
MATERIALS
www.advopticalmat.de

REVIEW

by vertical shifting the output waveguides with respect to the input one, it is possible to achieve any required splitting ratio of the SPP signal.[86]

A number of alternative splitter designs was proposed for DLSPPW circuitry. The discussed above fork-shaped design can be modified by making one output arm physically separated from the input waveguide to obtain an asymmetric splitter.[129] A family of splitters is based on the strong coupling of the DLSPP waveguides located at small distances from each other (Figures 11e) allowing inter-waveguide mode coupling.[86] For these two approaches, however, precise fabrication is needed to obtain required characteristics with reasonable accuracy. On the other hand, a numerically demonstrated splitting approach based on multimode interference[128] (Figure 11f) is very robust in terms of fabrication, but for the price of a fixed arm separation defined by the SPP interference pattern along with an increase of the required length and, consequently, higher absorption losses. Such a splitter was used for the experimental demonstration of signal demultiplexing in DLSPPW circuitry.[130]

After successful demonstration of efficient DLSPPW mode splitting, a Mach–Zehnder interferometer was developed composed of a Y-splitter followed by two parallel waveguides sections, which were recombined by a mirrored Y-splitter. Since in the symmetric Mach-Zehnder interferometer the path lengths of the two waveguide arms are identical (Figure 11g), constructive interference in the output is expected (Figure 11h): SNOM images indeed demonstrate efficient splitting and recombination of the DLSPPW signal. With the arm length of $l \approx 45$ μm for operational wavelength of $\lambda = 1550$ nm, the MZI has a transmission of about 20%. Due to the overall length of the Mach-Zehnder interferometer, the losses are largely dominated by the DLSPPW mode absorption accounting for ≈74% of the total loss.

4. DLSPPW Wavelength-Selective Components

To fully exploit the advantages of the plasmonic approach for broadband data transfer in highly integrated photonic circuits, such as wavelength multiplexing, and to achieve active functionalities, wavelength-selective components are needed. In this section we will overview various designs and performance of such components based on the DLSPP waveguides.

4.1. Bragg Reflector

One of the most widely used method for the wavelength separation and selection is based on diffraction on periodic structures. The examples include the wavelength rejection or filtering, implemented, for example, in high-reflectance interference mirrors, high-extinction interference filters or fiber Bragg gratings used for various sensing applications.[131] Various methods of the implementation of a Bragg reflector in a DLSPP waveguide were proposed and numerically investigated.[86] A compact Bragg reflector can be achieved by the variation of the waveguide ridge height (**Figure 12**a). With a five-period component, the reflectivity did not exceed $R \approx 0.5$ even for an optimized Bragg period, due to the required large height modulation, leading to strong free-space scattering. As an alternative design,

a Bragg reflector was implemented on the basis of square-wave or sinusoidal modulation (up to 20%) of the refractive index of the stripe (Figures 12b,c). A 20-period reflector, optimized by varying the high-refraction section length and the overall period, provides reasonably high reflectivity of $R \approx 0.7–0.8$. Such high refractive index modulation is experimentally challenging, while the reflectors with lower modulation need to be rather long (tens of periods). From all the proposed designs of a Bragg reflector, the one based on a metallic stripe Bragg grating under the polymer waveguide ridge provided the best performance with almost 90% of the SPP mode energy reflected using 11 μm Bragg reflector containing nine periods (Figure 12de).

A Bragg filter design based on variation of the waveguide width was also proposed.[132] The variation of the waveguide width introduces the change of the effective index of the mode. This makes it related to the Bragg reflector design based on the modulation of the refractive index discussed above (Figure 12b), but with a crucial advantage of a large modulation contrast. The DLSPPW effective mode indexes in the narrow and wide sections are ≈1.2 and ≈1.4, respectively. With a 50% Bragg filter duty cycle, this results in a transmission minimum at a wavelength of 1560 nm. SNOM characterization of the SPP mode reflection from a 30-period Bragg filter shows well-defined Bragg reflection accompanied by transmission extinction (bandgap) in the wavelength interval from 1540 to 1600 nm (Figures 12f–j). Relatively low transmission levels (≈0.3) observed outside of the band gap are partially accounted for by the DLSPPW mode propagation loss reducing the transmission by the factor of ≈0.7 on its own, the rest is related to out-of-waveguide scattering at the ridges.

4.2. Waveguide Ring Resonator

A compact and highly efficient wavelength-selective component for integrated photonic circuits is a waveguide ring resonator (WRR, **Figure 13**a–c). It is formed by a waveguide loop placed in the vicinity of a straight waveguide. When the input mode is passing the region adjacent to the ring, it is partially coupled to the waveguide forming the ring. The mode transferred in the ring starts to circulate around it, after each turn being partly decoupled back into the straight waveguide. The resulting interference of the directly transmitted and passed through the ring SPPs depends on the phase delay acquired by the mode traveling a complete circle around the ring, or in other words on the number of the mode wavelengths λ/n_{eff}^{ring} which can be placed along the ring circumference. Therefore, for different wavelengths, different WRR transmission will be observed, resulting in a quasi-periodic wavelength dependence of the WRR transmission featuring sharp minima (Figure 13h). The radius of the ring defines the periodicity, while the gap between the ring and the straight waveguide defines the coupling strength, in a way similar to one described in Section 2, and hence the modulation contrast between the transmitting and blocking WRR states[133] (cf. red and blue lines in Figure 13h). The WRR transmission can be expressed as

$$T = \frac{\alpha^2 + t^2 - 2\alpha t \cos\theta}{1 + \alpha^2 t^2 - 2\alpha t \cos\theta} \tag{6}$$

where

ADVANCED
OPTICAL
MATERIALS
www.advopticalmat.de

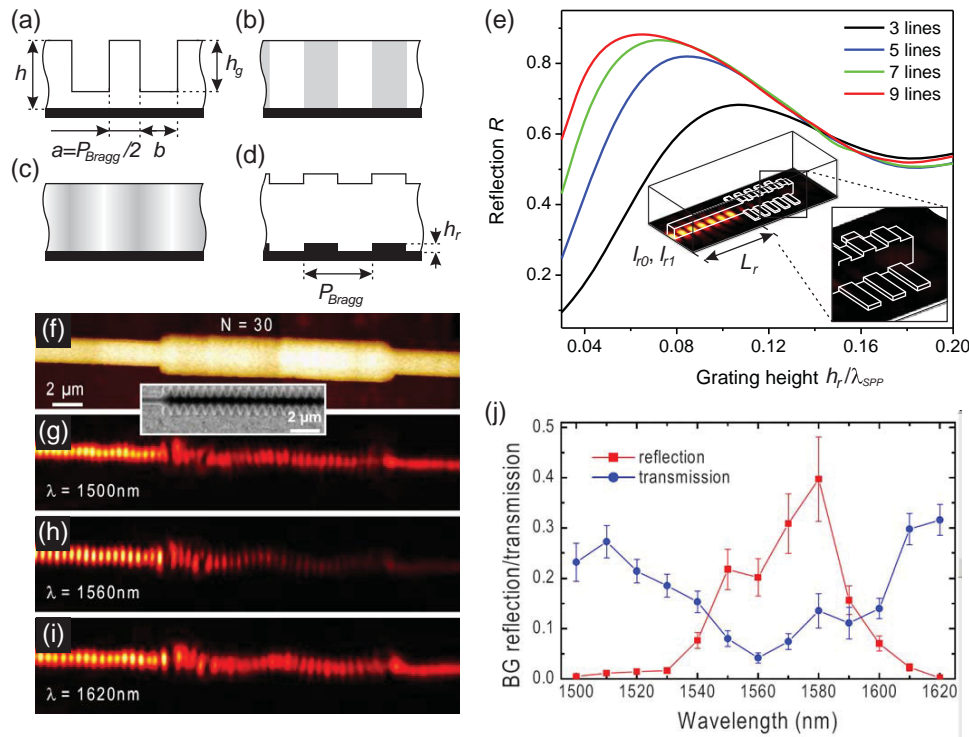Materials
Views
www.MaterialsViews.com

REVIEW

Figure 12. Bragg reflector based on a) periodic modulation of the waveguide height, b) square-wave and c) sinusoidal modulations of the dielectric refractive index, and d) rectangular metal stripe grating. e) Dependence of reflectivity R of the rectangular metallic grating on the grating height h_y for different number of periods for a 600 nm × 600 nm polymer-based DLSPPW operating at $\lambda = 1550$ nm. The inset shows the simulation setup. Adapted with permission.[86] Copyright 2008, Optical Society of America. f) Topography and g–i) near-field optical images of the 18 μm long Bragg filter with the period of 600 nm for different wavelengths: g) 1500 nm, h) 1560 nm, and i) 1620 nm. Inset shows an SEM image of the Bragg grating section. j) Reflection and transmission spectra of the Bragg filter determined from the near-field images. Adapted with permission.[132] Copyright 2009, American Institute of Physics.

$$\theta = \left(2\pi / \lambda\right) n_{eff}\left(\lambda\right) 2\pi r + \phi \qquad (7)$$

and t is the amplitude transmission coefficient for the straight waveguide mode directly passing the coupling region, α is the amplitude attenuation of the mode during a single circulation around the ring, λ is the free-space wavelength, r is the ring radius, $n_{eff}(\lambda)$ is the wavelength-dependent mode effective index, and ϕ is the coupling-induced phase shift caused by mode perturbation in the coupling region[134] (in the first approximation it can be omitted). An alternative point of view which leads to the same result is to consider a superposition of the SPP waves circulating in the ring as a ring-resonator mode, though strongly coupled to the straight waveguide.

DLSPP WRRs having a radius of only 5 μm exhibit a very efficient ring-mode excitation and well-pronounced wavelength-dependent behavior around a wavelength of 1550 nm for the edge-to-edge gaps between the ring and the straight waveguide below approximately 600 nm (Figure 13).[132] The experimental spectra are well described by a theoretical dependence (Equation (3)) with calculated effective index dispersion $n_{eff}(\lambda) \cong 1.61 - 0.25\lambda\,[\mu m]$ and the WRR parameters $\alpha \cong 0.55, t \cong 0.7,$ and $R \cong 5.43\,\mu m$ (Figure 13h). The investigated WRR features nearly complete extinction of the mode, reaching attenuation values of ≈13 dB at 1590 nm with about 20 nm bandwidth.

As was discussed above, the coupling between DLSPP waveguides is highly dependent on the separation distance between

them. As a consequence, the wavelength-selective characteristics (particularly the depth on the resonance dip) are very sensitive to the fabrication precision of the WRR coupling region. To diminish the influence of the fabrication uncertainties, the resonating waveguide loop can be made in a form of a racetrack (two semicircles connected by straight waveguide sections parallel to the straight input waveguide). In this case the interaction length between the waveguide and the resonator is longer, and keeping the same coupling efficiency as in the case of the ring shape, the racetrack can be moved further, so the same fabrication error will have a smaller relative influence.[135] Another approach, which increases the tolerance of the structure performance to the fabrication uncertainties is to use a disc resonator instead of the ring; in this case the precise fabrication of the ring width is not needed.[136,137]

4.3. Directional Coupler

As was discussed in Section 2, the mode from a DLSPP waveguide can be efficiently transferred to a neighboring waveguide if the separation between them is sufficiently small. The coupling length (the length needed for the total energy transfer from one waveguide to another) depends on the DLSPPW mode profile, which in its turn is wavelength-dependent. This effect can be used to realize a wavelength-dependent directional coupler
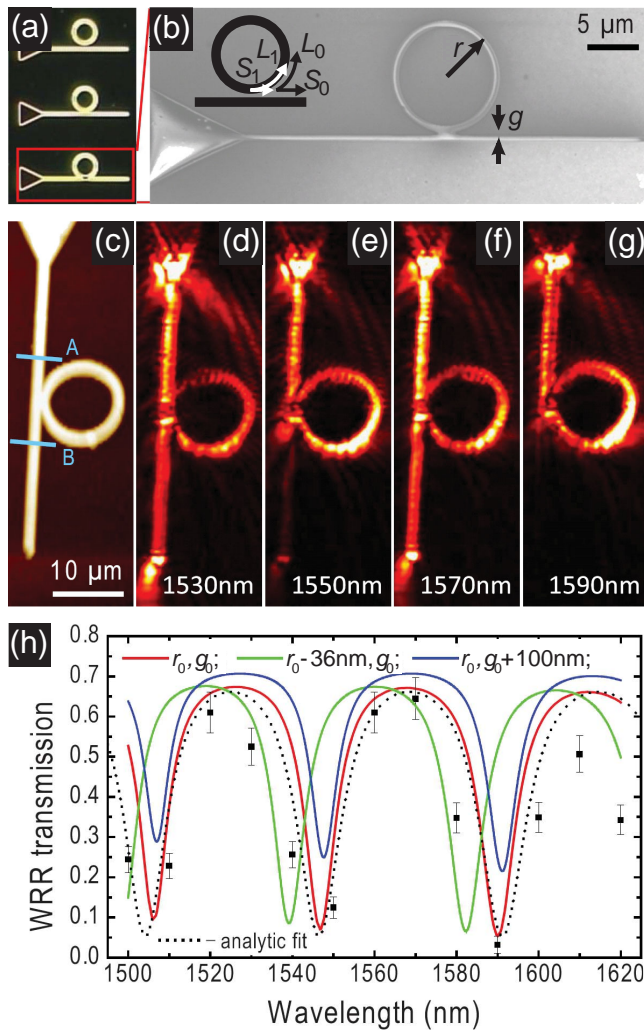
www.MaterialsViews.com

ADVANCED
OPTICAL
MATERIALS
www.advopticalmat.de

REVIEW

Figure 13. a) Dark-field microscope image of WRRs with different coupling gaps. b) SEM, c) topography and d–g) near-field optical images of a WRR for different wavelengths: d) 1530 nm, e) 1550 nm, f) 1570 nm, and g) 1590 nm. h) WRR transmission spectra determined from near-field images together with the analytic fit by Equation (6) and the numerical simulations. Three sets of WRR parameters were considered for the ring radius and gap width of $R_0 = 5486$ nm and $g_0 = 250$ nm, $R = 5450$ nm and $g_0 = 250$ nm, and $R = 5486$ nm and $g = 350$ nm with a 10 μm-long input-to-output propagation distance (marked by lines A and B in (c)). Adapted with permission.[132] Copyright 2009, American Institute of Physics.

is practically wavelength independent maintaining the level of ≈0.23, a value that is consistent with the loss incurred for a 25-μm propagation distance (≈40%) and two S-bends (≈35% per bend). As expected, for shorter wavelengths, at which the mode localized stronger, the coupling is weaker and the coupling length is larger (Figure 14f).

The obtained dependence of the coupling length was used for the development of the purpose-designed DCs. Generally, with only one waveguide being excited at the input, the output signals, i.e., straight T_s and cross T_c transmissions can be represented as

$$\left\{ \begin{array}{c} T_s\ (\lambda) \\ T_c\ (\lambda) \end{array} \right\} = (T_{bend})^2 \exp\left(-\frac{L_p}{L_{prop}}\right) \left\{ \begin{array}{c} \cos^2 \\ \sin^2 \end{array} \left(\frac{\pi L_i}{2L_c\ (\lambda)}\right) \right\} \qquad (8)$$

where the first factor reflects the S-bend transmission, the second one reflects the power loss during propagation through the straight waveguide section of length L_p, and L_i denotes the effective interaction length ($L_i > L_p$ due to additional mode coupling in the S-bend regions[139]). The interaction length was evaluated to be $L_i \approx 34$ μm, so that it is possible to obtain the wavelength division characteristics for any given DC length and, therefore, by choosing the appropriate values to design a DC structure that would ensure spatial separation of signals corresponding to different wavelengths. For example, an increase of the length of parallel section by ≈5.5 μm for the DC with $d = 1000$ nm would enable spatial separation of the wavelengths of 1400 and 1620 nm, belonging to E and L telecommunication bands (Figure 14g).

5. DLSPPW Active Components

As has been shown in the previous sections, the DLSPPW approach proved to be efficient in guiding and passive manipulation of plasmonic signals. However, we will only be able to speak about plasmonics in the same way as we speak about optoelectronics, if active plasmonic components are designed and demonstrated.[140–142] In this section, we will discuss various active functionalities realized on the DLSPPW platform, such as switching, modulation and active routing of plasmonic signals. The crucial advantage of the plasmonic approach, relying on high confinement level of plasmonic modes and excellent guiding characteristics of plasmonic waveguides, is a small size of active plasmonic components, which leads to high potential operational speeds and small energy consumption.

5.1. Design and Optimization of DLSPPW Active Components

As was discussed in Section 4.2, transmission through the ring resonator is determined by a phase shift acquired by the mode in the ring during a round-trip, which depends on its effective index n_{eff} (Equations (6) and (7)) and, therefore, on the refractive index of the ring material. With a pronounced sharp minima in the spectral characteristics (**Figure 15**a), this naturally gives the opportunity to use a WRR as an active switching component. Adjusting the ring radius so

(DC) component (**Figure 14**a,b). The length of the waveguides can be chosen so at a given wavelength after few oscillations between the waveguides, the mode can be fully localized in one of them, while for mode at another wavelength, having longer (or shorter) coupling length, the number of oscillations may be such that the mode will be fully localized in another waveguide. Directional couplers, comprising input and output S-bends have been realised[138,111] (Figure 14). As predicted by the theory (Section 2), the coupling length L_c was found to have a strong dependence on the separation distance (cf. Figures 14c,e) and also to vary noticeably with the wavelength, influencing the power ratio between the output waveguides (cf. Figures 14c,d). At the same time, the sum of power flows in the output channels

ADVANCED
OPTICAL
MATERIALS
www.advopticalmat.de

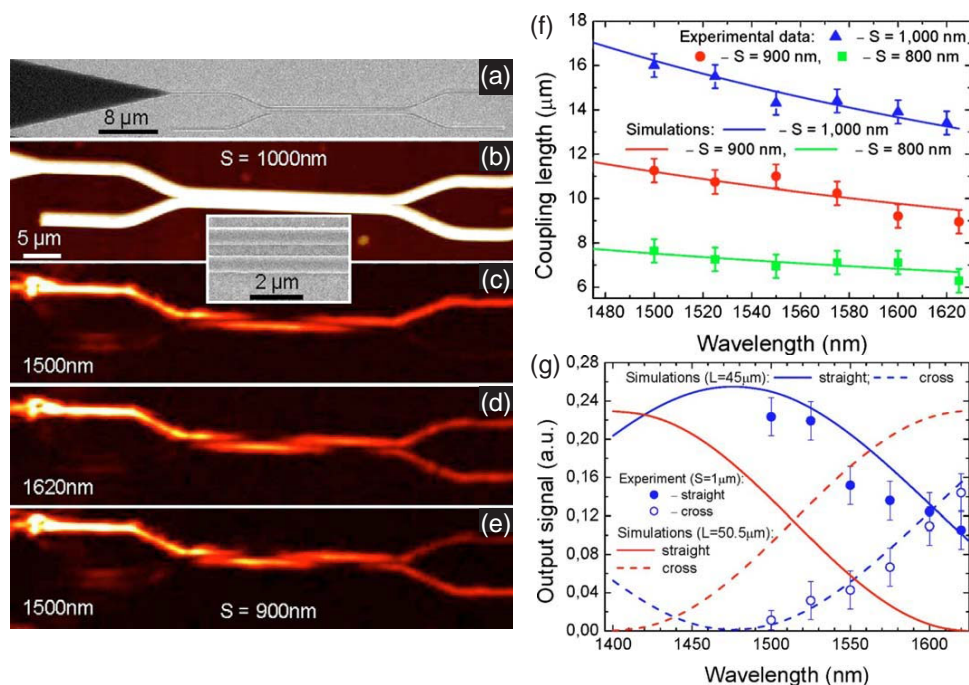REVIEW

www.MaterialsViews.com

Figure 14. a) SEM image of the DC with a funnel structure for the DLSPPW excitation. b) Topography and c–e) near-field optical images of 45 μm long DCs with the separations b–d) $d = 1000$ nm and e) $d = 900$ nm for different wavelengths: c) 1500 nm, d) 1620 nm, and e) 1500 nm. The inset shows an SEM image of the coupling region for $d = 1000$ nm. f) DC coupling length L_c evaluated for different wavelengths and separations from the SNOM images (data points) and with numerical simulations (curves). g) DC output signal normalized with respect to the input, determined from the near-field images and calculated using Equation (5) with the DC coupling length dispersion shown in (f). Adapted with permission.[138] Copyright 2009, Optical Society of America.

that the signal wavelength is located at the steepest slope of the transmission (red arrow in the figure), one can change the refractive index of the ring material via thermo-optic, electro-optic, or optically-induced nonlinear effects. Even with minute changes in the refractive index of the ring material, a related small shift in the resonances will lead to significant changes in the transmission at the signal wavelength (inset to Figure 15a).[143]

Although the general principle of active WRR operation is very clear, the optimization of the WRR design, e.g., finding the ideal ring radius, is not so straightforward. With the increase of the ring radius the refractive index changes will produce larger phase shifts; at the same time this will result in higher losses which will reduce the maximum WRR transmission and, therefore, the steepness of the resonance slopes, decreasing the modulation depth. Additionally, this will also increase the component size. To account for this different trends, a figure of merit for an active WRR was introduced, benchmarking its performance and the integration level:[144]

$$M_{WRR} = \frac{\partial T/\partial n}{R/\lambda} = 4\pi^2 \frac{\partial T}{\partial \theta} \frac{\partial n_{eff}}{\partial n} \qquad (9)$$

The high figure of merit corresponds to strongest change in the WRR transmission with the refractive index of active material $\partial T/\partial n$ for the smallest possible size R of the resonator. One can recast the expression so that M_{WRR} is defined through a new set of parameters: $\partial T/\partial \theta$ which is determined by the geometrical parameters of the structure and $\partial n_{eff}/\partial n$ which

is the rate of change of the effective index of the SPP guided mode in the resonator with the change of the refractive index of the dielectric material. The latter term is always greater for SPP modes due to the field confinement and enhancement in plasmonic waveguides than for photonic modes in all-dielectric waveguides. For each radius (corresponding to a certain losses α), the highest value of derivative $\partial T/\partial \theta$ can be found using Equation (6) by varying the transmission coefficient t, determined by the ring-waveguide gap g, and the dependence of the FOM on the radius r can be recovered (Figure 15b). One can see that for an active WRR based on a single-mode polymer-based DLSPPW, there is an optimal radius ≈6 μm. The refractive index change of just $\Delta n \approx 5 \times 10^{-3}$ in the optimized design results in a drastic (≈5-fold) change in the WRR transmission (Figure 15a).

For comparison, one can consider an active component based on a Bragg reflector (the same design as in Figure 12d,e, with a straight waveguide section after the component as an output).[143] With the grating period adjusted so that the signal wavelength is at the edge of the bandgap (but still inside it), the induced changes in the ridge refractive index as small as 10^{-2} (possible, e.g., via a thermo-optic effect) can shift the band structure of the Bragg grating so that at the considered wavelength the signal SPP will be in the transmission band. This effectively changes the Bragg filter transmission and opens the way to DLSPPW signal modulation. In the case of an MZI with an arm length of $l \approx 45$ μm, the change of the effective index of the mode in one arm needed to achieve a complete extinction is $\Delta Re(n_{eff}) = \lambda/(2l) = 1.72 \cdot 10^{-2}$.[116]

www.MaterialsViews.com

ADVANCED
OPTICAL
MATERIALS
www.advopticalmat.de

REVIEW

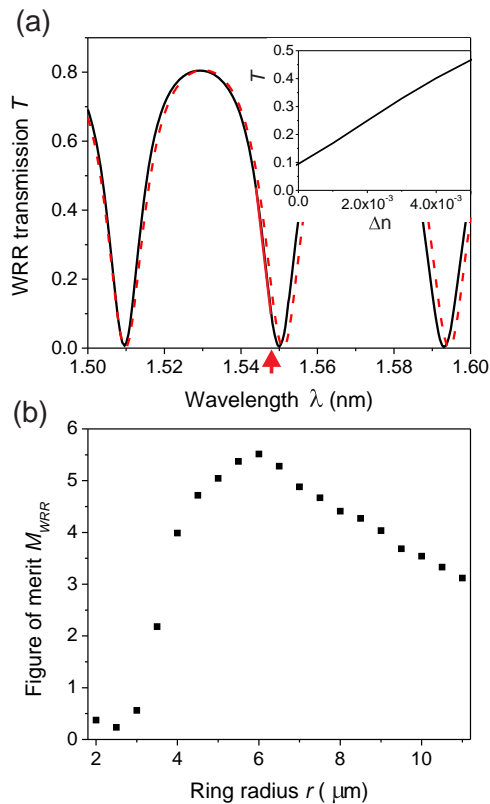**Figure 15.** a) FEM numerical simulation of the wavelength-selective transmission of the SPP mode through a WRR with a radius $r = 5.5$ µm and an edge-to-edge distance between the ring and the input waveguide $g = 160$ nm. Solid black curve represents numerical simulations, dashed red curve is the analytical fit using Equations (6) and (7). The red section of the curve shows the region with the steepest slope in transmission, while the red arrow shows the choice of the operation wavelength for the active device. b) WRR figure of merit M_{WRR} as a function of the ring radius r calculated using Equation (9).

5.2. Optically Controlled WRR Component

Optically-controlled components on the basis of WRRs were introduced using a ring resonator based on a polymer DLSPPW doped with disperse red 1 (DR1) dye to achieve the nonlinear response (**Figure 16**a–e).[145] Azobenzene chromophores, such as DR1, are attractive materials for studying various second order nonlinear optical effects and polarized light-induced anisotropy. Control light with a frequency near the main absorption resonance (490 nm) causes the azobenzene molecule to change from the *trans* to the *cis* configuration. This results in a substantial change in a molecule's dipole moment and, hence, the polarizability and refractive index of the material (Figure 16f). Both fast picosecond-scale processes due to molecular transformation and much slower processes of molecular photo-orientation, takes place when the control light is linearly polarized and results in pronounced light-induced anisotropy.[145]

The typical dynamic switching may lead to the photo-induced changes as high as $\Delta n = 3.7 \cdot 10^{-3}$. Such large changes in the refractive index of the ring material are more than sufficient for significant modulation of the WRR transmission, as was observed experimentally in agreement with numerical simulations.[145] The introduction of the control light was initially followed by a rapid decrease in the WRR transmission, which slowed down at higher powers due to the saturation of the DR1 molecular response (Figure 16g). The total transmission changes by more than 50% were observed, which is in good agreement with the simulations (Figures 16d,e). The switching is reversible, the transmission returns to the high level after unpolarized white-light illumination. This suggests that the dominating role in the nonlinear response is the molecular reorientation processes leading to the refraction index changes. While the observed ON/OFF switching time is low for real-time signal modulation and routing, the discussed above active WRR component has been proposed for designing of optically reconfigurable photonics circuits.

An alternative approach to optical DLSPPW mode switching in a directional coupler geometry using photo-thermal effect in the polymer doped with gold nanoparticles was experimentally demonstrated and a modulation depth of almost 100% in both source and cross DLSPPW channels (these signals are in antiphase) was observed.[146]

5.3. Electro-optic DLSPPW Switches

In order to achieve the electro-optic functionality with a WRR, the design was further developed to include the control electrodes via patterning a metal film (**Figure 17**a,b).[147] The same DR1 molecules used for the optically controlled component described in Section 5.2 were employed as a doping material due to a large r_{33} coefficient, which is related to the properties responcible also for the optical nonlinearity. For low applied control voltages, the WRR transmission shows a significant increase, but after the electric field increases above 8 MV m^{-1}, the transmission recovers to the initial value (Figure 17c). This was hypothesized to be the result of the structural deformation in the PMMA structure due to the electrostrictive effect. Time-resolved measurements using square-wave 25 MV m^{-1} electric field show fully-reversible electro-optical modulation of the DLSPPW signal with a 18% modulation depth (Figure 17d). The response time of the transmission modulation is on a different time-scale, which is in favor of electrostrictive nature of the effect. Interestingly, undoped-PMMA-based WRRs exhibit a 14% modulation depth, but their response time is ten times slower. This can be understood considering the modification of PMMA plasticity by the DR1 doping. The underlying switching mechanism can then be the combination of electrostrictive and electro-optic effects. An alternative design with the second electrode at the top of the ring,[144] being more efficient, is more challenging in terms of fabrication.

An interesting approach for modulation in DLSPPWs is based on the implementation of the DLSPPW dielectric core as a channel filled with nematic liquid crystal. Utilizing an electro-optic effect in the directional coupler geometry, signal modulation with an extinction ratio of 12 dB was theoretically demostrated.[148] Finally, we note that conventional electro-optic materials provide too small refractive index modulation to be used in highly-integrated active components. Novel nonlinear polymers,[68] naturally compatible with the DLSPPW technology, can pave the way for DLSPPW-based modulators operating in
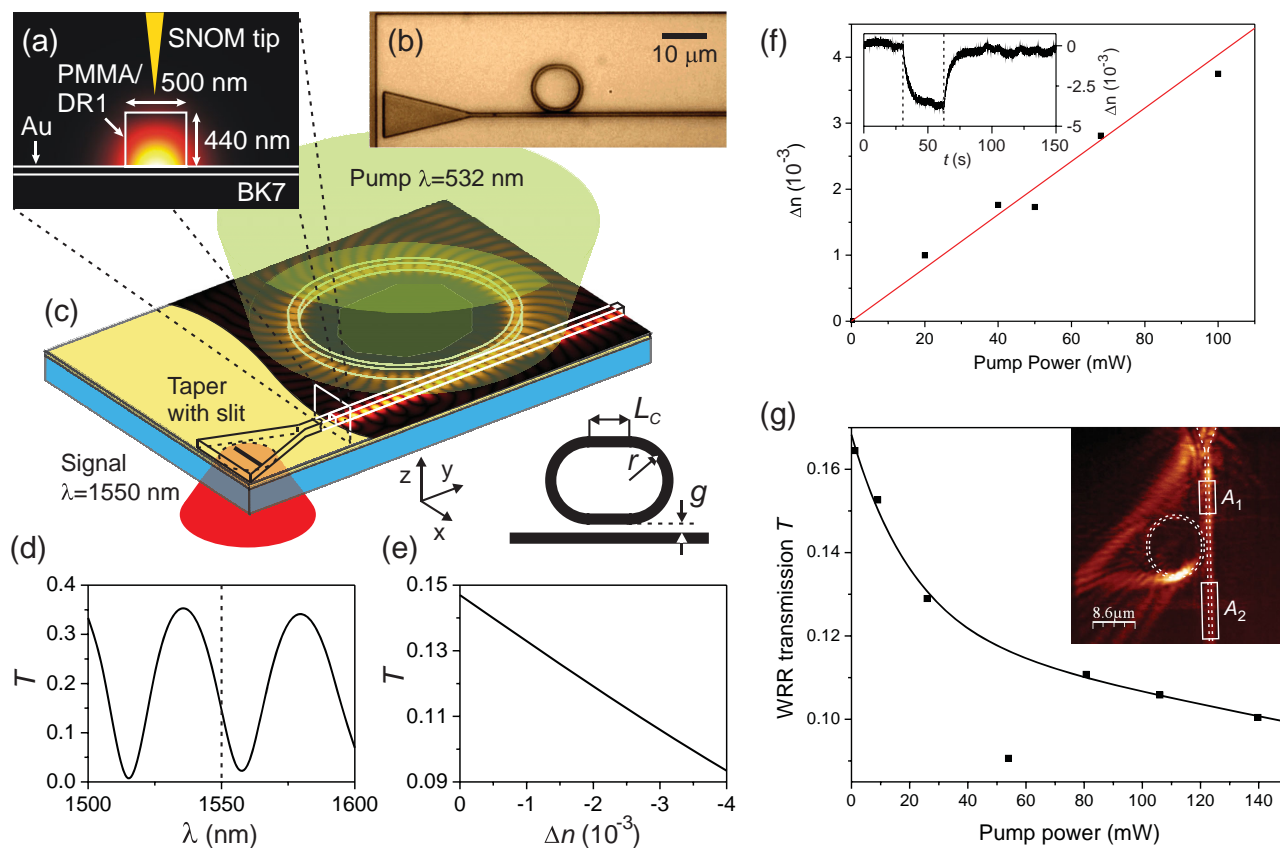
Figure 16. a) Cross-section of a polymer-based DLSPP waveguide for the WRR implementation with the simulated P_y power flow profile of its fundamental TM_{00} SPP mode. b) Optical image of a PMMA/DR1 ring resonator. c) The experimental setup with the signal and control light beams. Incorporated in the sketch is the simulated $\left|Re(E_z)\right|$ field map of the SPP mode at a distance of 10 nm above the metal surface. d) The wavelength dependence of the transmission of the SPP mode through the WRR with $R = 4.971$ µm, $g = 185$ nm, $L_c = 1$ µm, the waveguide parameters are as in (a). e) Dependence of the SPP mode transmission T on the change in the refractive index of the ring simulated for $\lambda = 1550$ nm (dashed line in (d)). f) The dependence of the refractive index change at $\lambda = 633$ nm in a 440 nm thick PMMA/DR1 film on the power of 532 nm control light. The inset shows the modulation dynamics for 110 mW control power, the 'on' and 'off' states of the control pulse are marked by the dashed lines. g) The dependence of the SPP mode transmission at $\lambda = 1550$ nm through the WRR on the control power. Inset: near-field intensity distribution of the SPP mode transmission through the racetrack resonator. Adapted with permission.[145] Copyright 2011, Optical Society of America.

MHz and GHz ranges and in this respect matching the performance of the photonic ones.[88] For example, a DLSPPW-based modulator with the design from Ref. [144] has the energy consumption per bit[149] $\Delta E_{bit} = (1/4)CV^2 \approx 20$ fJ (calculated using estimated device capacitance of $C = 1.3$ fF and the required control voltage of $V = 7$ V), which favorably compares with the best values for photonic[88] and plasmonic[68,150] modulators.

5.4. Thermo-optic DLSPPW Switches

DLSPPW active components utilizing a thermo-optic effect are the most investigated.[151] PMMA polymer, which is typically used for a DLSPPW dielectric core, has an intrinsic large thermo-optic coefficient of $(\partial n / \partial T)_{PMMA} = -1.05 \cdot 10^{-4}$ K^{-1}. Hence, a moderate temperature increase by 50° results in a refractive index change as high as Δn on the order of 10^{-3}, allowing DLSPPW signal modulation in components of various designs. Furthermore, the effect can be at least 3 times magnified by using alternative materials, such as CAP (see below).[152] The temperature change can be induced using resistive heating

in the same metal film that supports the SPP mode and is located beneath the core. Therefore, the refractive index change is induced in an efficient way in the dielectric region where the SPP mode has the highest intensity, exactly where it is needed. This is different in the case of thermo-optical components based on dielectric waveguides, where the electrodes are located far in the cladding, and, thus, temperature induced changes are generated far from the mode and their influence it much weaker.

The first designs of thermo-optic DLSPPW components were again based on the WRR geometry (**Figure 18**a).[95,114,151–153] A PMMA-based ring resonator was resistively heated by a current passing through a metal strip under the structure. The temperature increase of 100 K resulted in a blue shift of the WRR resonances by ≈4.5 nm. Due to high quality factor of the fabricated structures and sharp resonance minima, this led to the changes in the WRR transmission of up to 9 dB at the wavelength of $\lambda = 1538$ nm corresponding to the steepest slopes in the wavelength characteristic (Figure 18b–d).

The WRR operation as an active component discussed above is based on resonant effects and, thus, has a narrow wavelength
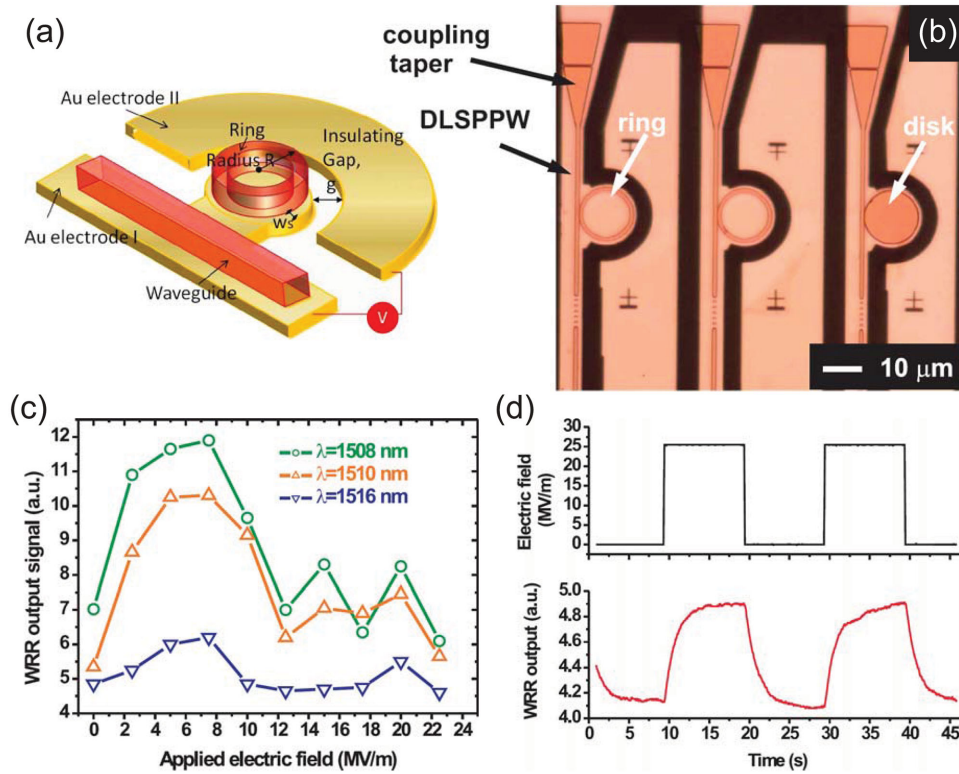
www.MaterialsViews.com

ADVANCED
OPTICAL
MATERIALS
www.advopticalmat.de

REVIEW

Figure 17. a) A design of the WRR with in-plane electrodes. b) Bright-field image of the ring and disk resonators fabricated on the Au electrodes. The dark area corresponds to isolating glass trenches separating the electrodes. c) Evolution of the WRR output signal at 1508 nm, 1510 nm, and 1516 nm for an upward voltage sweep. d) PMMA-DR1 WRR output response time for an electric field step of 25 MV m^{-1}. Reproduced with permission.[147] Copyright 2012, Optical Society of America.

bandwidth. On the other side, if the broadband operation of the switch is needed, a classical design based on a Mach–Zehnder interferometer is beneficial (Section 3). When a phase delay ϕ is introduced in one arm of the MZI by an external control signal, the interference of the signals propagating in two arms can be changed and efficient signal modulation can be achieved: destructive interference and a zero signal output can be obtained if $\phi = \pi$ is introduced. The induced phase $\varphi = 2\pi/\lambda \cdot \Delta nL$ is a weak function of the wavelength, therefore, the modulation can be equally efficient in a broad wavelength range. This makes an active MZI useful for broadband signal switching, at the price of a larger required size ($\approx$50 µm) than that of the WRR due to sufficiently long arms needed for accumulating a phase difference at realistic refractive index changes.

Electrically driven modulation of the MZI output signal via resistive heating of one of the arms was demonstrated (Figure 18e).[152] It was fabricated with a CAP polymer as a dielectric load, having a large thermo-optic coefficient $(\partial_n/\partial T)_{PCAP} = -3\cdot10^{-4}$ K^{-1}, 3 times larger than that for PMMA. This has allowed to achieve the phase shift up to $\approx$2π, which led to high modulation depths and even to a double switching (Figure 18f). Not complete signal extinction is related to the distortion of the amplitude and the zero-voltage phase by the presence of the electrode gaps, so that the equal-amplitude condition for zero-output destructive interference is not satisfied. The modulation depth can be increased to 100% by adjusting the splitting ratio to restore equal power levels at the arms

outputs. As an additional advantage, CAP's specific heat coefficient (amount of heat required to change the material's temperature) is 270 times lower than PMMA, which allows decrease of the switching times to a microsecond range. The heating-up and cooling-down times were measured to be approximately 20 and 15 µs, respectively, so that the operation frequency of the device is about 50 kHz at a 3 dB cut-off level (Figure 18g).

The power required to switch the MZI, apart from geometrical parameters, is greatly influenced by thermal conductivities of the DLSPPW ridge and substrate materials. These parameters define how the available heating power is divided between the DLSPP waveguide and the substrate. For example, for the substrate with a high thermal conductivity, the supplied heat will be mainly dissipated through the substrate, therefore, high switching powers are needed. Here, the choice of a low heat-conductive CYTOP substrate ($\kappa_{CYTOP} = 0.12$ W m^{-1}K^{-1}) results in a 10-fold decrease of the switching power in comparison to a MgF$_2$ substrate ($\kappa_{MgF_2} = 11.6$ W m^{-1}K^{-1}), resulting in milliwatt switching powers of the MZI. The actual power required for the MZI switching is actually even smaller than that in Figure 18f. Taking into account that only a fraction of the total power is dissipated in the MZI arm region, the switching power P smaller than 3 mW was estimated to be sufficient for the actual switching process for an almost 100% modulation contrast. This corresponds to the energy consumption of the order of $\Delta E_{bit} = P\tau_{rise} = 60$ nJ per bit, where $\tau_{rise} = 20$ µs is the modulation signal rise time.[152]

**ADVANCED
OPTICAL
MATERIALS**

www.advopticalmat.de
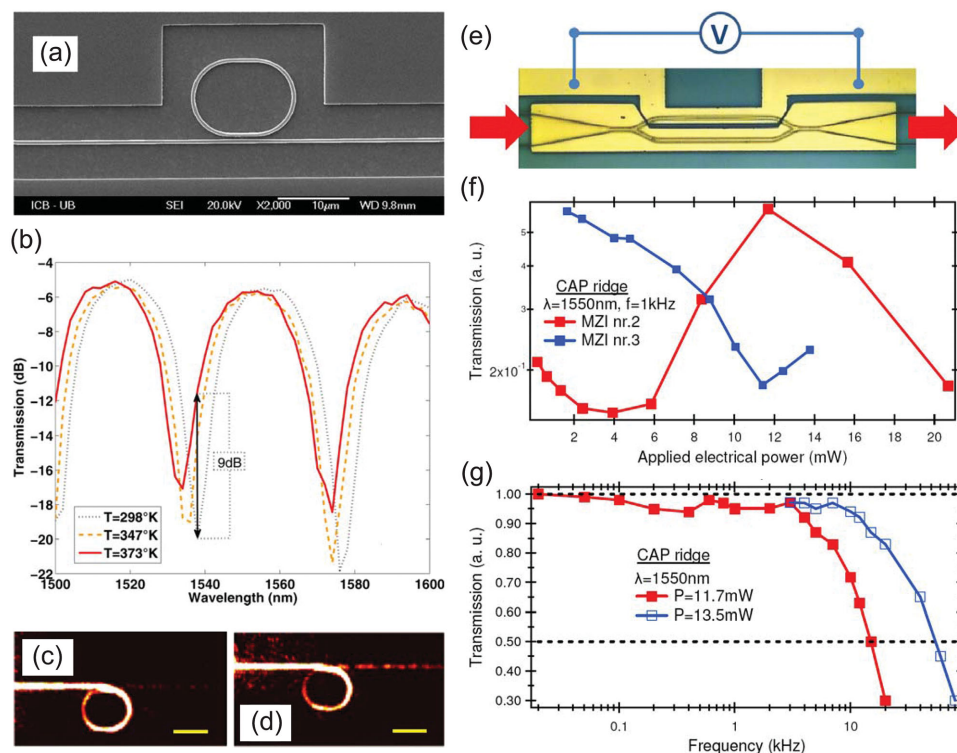
**Materials
Views**

www.MaterialsViews.com

REVIEW

Figure 18. a) SEM image of a DLSPPW racetrack resonator fabricated with PMMA on a thin gold film. b) Transmission spectra of the resonator in (a) for different temperatures. c,d) LRM images of a race-track resonator ($R = 5.8$ µm, $L = 2.5$ µm, edge-to-edge racetrack-waveguide gap $G = 240 \pm 40$ nm) recorded at $\lambda = 1538$ nm at c) 298 K and d) 373 K (scale bar is 10 µm). Reproduced with permission.[95] Copyright 2011, American Institute of Physics. e) Mach–Zehnder interferometer with the end-fire in- and out-coupling components. The resistive-heating voltage is applied to the electrodes. f) Dependence of the CAP-polymer-based MZI transmission at $\lambda = 1550$ nm on the applied electric power for two measured structures. g) Dependences of the MZI transmission at $\lambda = 1550$ nm on the modulation frequency. Reproduced with permission.[152] Copyright 2012, Optical Society of America.

The requirements on the electrode design and the electric isolation have an impact on the operation wavelength bandwidth and should be carefully considered. Due to the presence of two electrode gaps, the electrically isolated arm section acts as a Fabry-Perot cavity for SPP modes if the reflection from the electrodes is significant. With multiple reflection at the edges, the transmission through the MZI depends on the wavelength in a periodic manner and so does the resulting transmission modulation.[152]

Exploiting the strong refractive index modulation achievable via a thermo-optic effect, a number of approaches for routing SPP signals have been proposed. Reversible switching of the mode between the outputs of a directional coupler via resistive heating of the coupling region was observed.[151] Alternative routing approaches, based on conventional designs of add-drop filters, i.e., single- or double-WRR structures, were investigated.[154] Low power consumption (down to a fraction of mW) and fast switching times (down to few µs) were experimentally demonstrated for switching the signal in silicon-on-silica photonic circuits with incorporated DLSPPW-based active components.[155,156]

6. Figure of Merit for Plasmonic Waveguides in Integrated Photonic Circuits

Following the advantages offered by the plasmonic approach in terms of field localisation and active control of the optical

signal, numerous plasmonic waveguiding geometries have been proposed (Figure 1). The designs cover the whole range of achievable mode sizes from tens of nanometers to micrometers, and related propagation lengths from sub-micrometer to centimeter scales. In fact, there is a general trade-off between these two characteristics: higher confinement usually corresponds to a larger portion of the mode propagating in the metal, which leads to higher losses and therefore a lower propagation length. In these circumstances, to compare the diverse variety of plasmonic waveguides, a figure of merit was introduced to quantitatively characterize their guiding performance.[157] As the best starting point, the figure of merit

$$M_1^A = 2\sqrt{\pi} \cdot \frac{L_{prop}}{\sqrt{S}} \tag{10}$$

represents a straightforward measure of the above-mentioned trade-off: a ratio between the signal propagation length L_{prop}, reflecting the propagation characteristic of the mode and the size of the mode $S^{1/2}$ (S is the effective mode area), reflecting its confinement. Although it has a clear physical meaning and gives a vivid characterization of the mode as such, it is not ideal for benchmarking the performance of the waveguide for the implementation in highly integrated optical circuits. The square root of the mode area in the denominator of M_1^A is effectively a measure of how closely parallel waveguides

www.MaterialsViews.com

ADVANCED
OPTICAL
MATERIALS
www.advopticalmat.de

REVIEW

can be packed on a chip. However, modes with the same effective areas can be coupled more efficiently or less efficiently to the neighboring waveguide depending on their spatial field distributions. Furthermore, it has been shown that there is a variety of ways to quantify the effective mode area, frequently giving essentially different and even opposite results.[158] Therefore, the above figure of merit was modified in order to include a direct measure of the coupling efficiency.[40,99] When two parallel waveguides are placed next to each other, their coupling leads to the tunneling of the mode from one waveguide to another with a full energy transfer after a distance L_{coupl}. With this in mind, the waveguide center-to-center separation d_{sep} corresponding to $L_{coupl}(d_{sep}) = 4L_{prop}$ will give a direct measure of the achievable integration density: after one propagation length (when mode intensity will decrease in ≈ 2.7 times), only 15% of the mode energy will be coupled in the neighboring 'aggressor' waveguide. Therefore, using the coupling distance approach, the figure of merit can be represented as[99]

$$M_1^B = \frac{L_{prop}}{d_{sep}} \qquad (11)$$

The second main parameter characterizing particularly the performance of a multi-branched waveguide circuit is an ideal radius, minimising signal loss along a curved waveguide section. This parameter defines the size of all circuit components, such as splitters, WRRs, MZIs, etc. The ideal waveguide radius is a trade-off between the Ohmic losses (higher for larger radii) and radiation losses (higher for smaller radii).[109] The figure of merit introduced as[157] $M_2 = 2L_{prop} \cdot (n_{eff} - n_{surr})$, where n_{eff} is the mode effective index and n_{surr} is the refractive index of the surrounding medium, gives only a partial answer. It takes into account only the radiation losses: the further the SPP mode dispersion from the light line, the lower the coupling efficiency to scattered light and, similarly, the further the SPP mode dispersion from the planar-surface SPP dispersion, the lower the coupling efficiency to unbounded SPPs. At the same time, with the value of such FOM fixed, the radiation losses are also influenced by the particular waveguide geometry. As an alternative solution, the all-inclusive figure of merit for multi-branched plasmonic circuitry was proposed, taking into account both Ohmic and radiation losses and directly estimating the waveguide bends performance:[40]

$$M_1^C = \frac{L_{prop}}{d_{sep}} \cdot \left(\frac{T(r)}{r}\right)_{max} \qquad (12)$$

where $(T(r)/r)_{max}$ is the maximum of transmission-to-radius ratio, found varying the bend radius. Here, as a universal building shape for both waveguide bends, splitters and ring resonators, we took the bending shape in a form of a circular arc. In more narrow case of waveguide bends and splitters, one can get approximately 10% improvement in performance (for reasonably high transmission levels) using sine-based shapes.[116,86]

The obtained figure of merit was derived using 'local' characteristics of the waveguide performance: the cross-talk between neighboring waveguides and waveguide bend performance. The most relevant to the practical applications, however, is the estimation of the global performance of the multi-branched

plasmonic circuit as a whole data communication architecture. The most general benchmark describing the performance from these prospective can be defined as a bandwidth per unit area achievable in the circuit divided by the power loss per unit area due to Ohmic and radiation losses. Considering the case of multi-branched circuitry containing both straight and curved waveguide sections, the following expression for such 'global' figure of merit can be derived:[159]

$$M_{pass} = B \cdot \frac{L_{prop}}{d_{sep}} \cdot \left(\frac{L_{prop}^{bend}(r)}{r}\right)_{max} \qquad (13)$$

where B is the waveguide single-stream bandwidth (Equation (5), with the characteristic length $L = L_{prop}$) and $L_{prop}^{bend}(r)$ is the mode propagation length along a waveguide curved section, influenced by both Ohmic and radiation losses. Strikingly, although the local (Equation (12)) and global (Equation (13)) figures of merit are derived from absolutely different perspectives, they reflect essentially the same dependences of the waveguide performance characteristics. The only difference is that in the former case the bend transmission-to-radius ratio $T(r)/r$ is maximized, while in the second the same should be done for the propagation characteristic of the section $L_{prop}^{bend}(r)/r$. At the same time, the global FOM includes important parameter—the waveguide single-stream bandwidth—which was completely disregarded before.

The derived global figure of merit was applied to evaluate the performance of the main types of plasmonic waveguides (**Table 2**). The relevant waveguide characteristics were found using 2D eigenmode and full 3D finite element numerical simulations. For a fair comparison all the waveguides were implemented on a gold material platform at telecommunication wavelength $\lambda = 1550$ nm. Additionally, in the case of a wire-MIM waveguide, Al was considered to make a comparison with the design from the original experiments. As expected, a trade-off between L_{prop} and d_{sep} is observed for all the waveguides. The propagation length along the ideally curved section L_{prop}^{bend} is a factor of 1.2–4 shorter than L_{prop}, while the ideal radius can be of the same order as the waveguide cross-section in the case of the most highly-integrated waveguides, or can be up to 3 orders of magnitude larger in the case of, e.g., long-range waveguides. Due to small interconnect lengths, if nonlinearity is neglected, the calculated bandwidth B reaches extremely high values of tens of Tb s^{-1}, corresponding to the signal carrying pulses containing just a few field oscillations. Thus, the single-stream bandwidth will practically be limited by the current electronic data modulation technology presently capable of 10–100 Gb s^{-1} modulation and detection rates, while the overall bandwidth can be substantially increased using WDM techniques.

An interesting universal trade-off can be observed from Table 2 for the characteristics of plasmonic waveguides of completely different designs: the cross-talk limited photonic integration of straight data lines can be different by 2 orders of magnitude, the bend radii can be different by 5 orders of magnitude, propagation lengths can be different by 4 orders of magnitude (cf. d_{sep}, r and L_{prop} parameters for, e.g., long-range and wire-MIM waveguides), but the global FOM values fall within 2 orders of magnitude interval for all considered waveguides. This, however, can be regarded as a considerable

Table 2. Benchmarking characteristics for various plasmonic waveguide and comparison of the performance of the waveguides using global figure of merit (Equation (13)).

Waveguide type/ Characteristic	B	L_{prop}	d_{sep}	L_{prop}^{bend}	r	M_{pass}
Long-range waveguide[160]	14 Tb s^{-1}	1.75 mm	12 µm	1.1 mm	3 mm	0.75 × 10^3 Tb s^{-1}
DLSPPW[116]	39 Tb s^{-1}	45 µm	1.8 µm	31.5 µm	6 µm	6.1 × 10^3 Tb s^{-1}
Hybrid waveguide	70 Tb s^{-1}[42]	45 µm[42]	1.05 µm[42]	38 µm[42]	2 µm[42]	56.9 × 10^3 Tb s^{-1}[42]
	20 Tb s^{-1}[161]	16.3 µm[161]	1.3 µm[161]	15.1 µm[161]	3.5 µm[161]	1.1 × 10^3 Tb s^{-1}[161]
Wire waveguide (asym. mode)[40]	61 Tb s^{-1} (InGaAs coat.)	310 nm (InGaAs coat.)	85 nm (InGaAs coat.)	110 nm (InGaAs coat.)	12.5 nm (InGaAs coat.)	2 × 10^3 Tb s^{-1} (InGaAs coat.)
	90 Tb s^{-1} (SiO$_2$ coat.)	1.2 µm (SiO$_2$ coat.)	200 nm (SiO$_2$ coat.)	123 nm (SiO$_2$ coat.)	12.5 nm (SiO$_2$ coat.)	5.3 × 10^3 Tb s^{-1} (SiO$_2$ coat.)
Wire-MIM waveguide 70 Tb s^{-1}[69]	139 Tb s^{-1} (Al)	420 nm (Al)	65 nm (Al)	196 nm (Al)	12.5 nm (Al)	14.1 × 10^3 Tb s^{-1} (Al)
	86 Tb s^{-1} (Au)	480 nm (Au)	60 nm (Au)	405 nm (Au)	12.5 nm (Au)	22.3 × 10^3 Tb s^{-1} (Au)

difference, and the derived figure of merit can indeed be used to benchmark the performance of waveguides of various designs. Furthermore, as can be seen from Table 2, the particular geometrical and material parameters can modify the figure of merit within the same waveguide type by at least 2 times, which makes it useful to optimize the performance of the waveguide of choice. Analyzing the results presented in Table 2, one can conclude that the DLSPPW has as good guiding efficiency as other plasmonic waveguides, at the same time having all the advantages in terms of fabrication and active functionalities, while its hybrid modifications demonstrate the best network performance in terms of the global figure of merit. It is also important to note that while FOMs provide a global overview of the generic performance of the various waveguides, practical requirements, such propagation length or mode confinement, should be considered for each application separately since they may be determining the design parameter space. Traditional silicon-on-insulator (SOI) technology provides the mode propagation distances L_{prop} on centimeter scale, practically limited by waveguide wall roughness.[162] For typical sizes of 1 cm long, 450 nm × 220 nm SOI waveguides, waveguide separation distances $d_{sep} \approx 1.2$ µm, waveguide bends $r \approx 1$ µm and the data bandwidth of $B \approx 3.2$ Tb s^{-1} can be estimated (cf. Table 2).

To make this discussion complete, we need to point out that using the same approach it is also possible to introduce a figure of merit for active waveguide components:[159]

$$M_{act} = A \frac{\Delta f}{P} \qquad (14)$$

where A is the absorption loss, Δf is the operational bandwidth and P is the power required for a switching event at a standard 3 dB level. At the same time, benchmarking of various active components is very design-specific and lies beyond the scope of this review.

7. Signal Amplification in DLSPP Waveguides

Although the propagation lengths of plasmonic waveguides are large enough to establish middle-range on-chip communication, it will be extremely beneficial to extend them to larger, long-range scales. This can be done through amplification of the plasmonic signal and will be discussed in this section. Further development of the amplification approaches have led to the development of integrated plasmonic lasers.[163]

7.1. Specifics of Plasmonic Signal Amplification

The general approach for amplification SPP waves[45] is straightforward with DLSPPWs: a dielectric at the SPP-supporting interface should be a gain medium. Upon optical or electrical pumping, the emitters near (around 100 nm) the metal surface can radiate directly in the SPP mode via stimulated emission, so that the mode will be amplified.[86] The dielectric core of the DLSPP waveguide contains the predominant part of the mode energy and can be used as an active medium upon doping it with lasing atoms, molecules or quantum dots.

The dynamics of the emission in the active medium in the presence of plasmonic effects is, however, more complicated than in conventional dielectric waveguides or optical fibres, and depends on the specifics of plasmonic wave amplification.[49] The exited state of the emitter has, in the presence of a plasmonic material, a variety of ways to radiate: photonic and plasmonic relaxation channels, as well as nonradiative near-field quenching into the metal.[60] This results in a spatial dependence of excited state life times, influencing gain dynamics, which should be taken into account in a rigorous way in the rate equations. The theory of SPP amplification was first developed for a long-range SPP waveguide[49] and then further extended to DLSPPW modes.[164,165] The problem of competition of the relaxation channels can generally be treated using a Green tensor formalism[164] or a rigorous Purcell factor mapping implemented in finite element method numerical simulations.[165]

In the case of optical pumping, the nature of plasmonic waveguides possessing metallic components, inevitably leads to a non-uniform spatial distribution of the pump intensity, which also adds complexity to the process of excitation and SPP emission in the gain medium, due to spatially-dependent

www.MaterialsViews.com

ADVANCED
OPTICAL
MATERIALS
www.advopticalmat.de

REVIEW

field profiles. If an SPP wave is used for pumping, the required field overlaps can be optimized ensuring the delivery of the highest pump intensity exactly where it is needed the most: at the same metal interface supporting the signal SPP mode, and the stimulated emission efficiency can be increased 10-fold.[166] The SPP pump is also advantageous from the point of view of integration, removing the need of the external illumination of the waveguide. It, however, poses challenges in ensuring that a SPP pump has sufficient propagation length in the waveguide to provide the required energy transfer to the signal SPP mode. Finally, it should be noted that the amplification of the propagating plasmonic waves presents an easier task than the amplification of their localized counterparts,[167] which may be a basis of nanoscale coherent light sources, the so-called 'spasers'.[168]

7.2. Amplification of DLSPPW Mode Using Optically Pumped Gain Medium

Amplification of a plasmonic mode in the DLSPP waveguide was experimentally demonstrated by introducing a gain material in the DLSPPW dielectric core. PbS quantum dots (QDs) with emission peak near the signal SPP wavelength of $\lambda = 1525$ nm were considered (**Figure 19**a).[169] Under the illumination of the entire DLSPPW structure with a low intensity 532 nm pump light, spontaneous emission of the quantum dots into the fundamental TM_{00} DLSPPW mode was confirmed (Figure 19b). Plasmonic amplification was then demonstrated by adding a signal SPP with the wavelength resonant to the PbS radiative transition and achieving stimulated emission. A substantial

increase of the apparent propagation length from 13.5 μm to 17 μm (approximately 25% increase) was observed (Figure 19c). The stimulated emission phenomenon, the signature of which is the narrowing of the signal spectrum,[61] was further confirmed by analyzing the width of the mode in the Fourier space (Figure 19d).[169] The idea of QD-assisted plasmonic amplification in DLSPP waveguides was later extended to shorter near-infrared[170] and visible wavelength ranges.[171]

7.3. SPP Amplification in Semiconductor-based DLSPP Waveguides Under Electric Pumping

Optical pumping approach requires the use of external powerful light sources, which is not always compatible with the highly-integrated plasmonic circuit architecture. Electrical pumping approach is better suited for direct integration with optoelectronic applications. To realize electrical pumping, the approach based on metal–semiconductor Schottky contacts has been proposed.[54] The plasmonic waveguide was formed by interfacing a plasmonic film with an active InAs ridge where the SPP amplification via population inversion upon electronic injection can be achieved in a Schottky contact (**Figure 20**a). The lattice-matched $AlAs_{0.16}Sb_{0.84}$ electric back-contact completes the electric circuit, while a low refractive index SiO_2 matrix insured high confinement of the plasmonic signal. The SPP waveguide was designed for a wavelength of $\lambda = 3.16$ μm, corresponding to the peak in InAs emission spectrum. With a width of 350 nm and a height of 2000 nm, it supports a highly localized (on the order of $\lambda/10$) fundamental DLSPPW-type TM_{00} mode
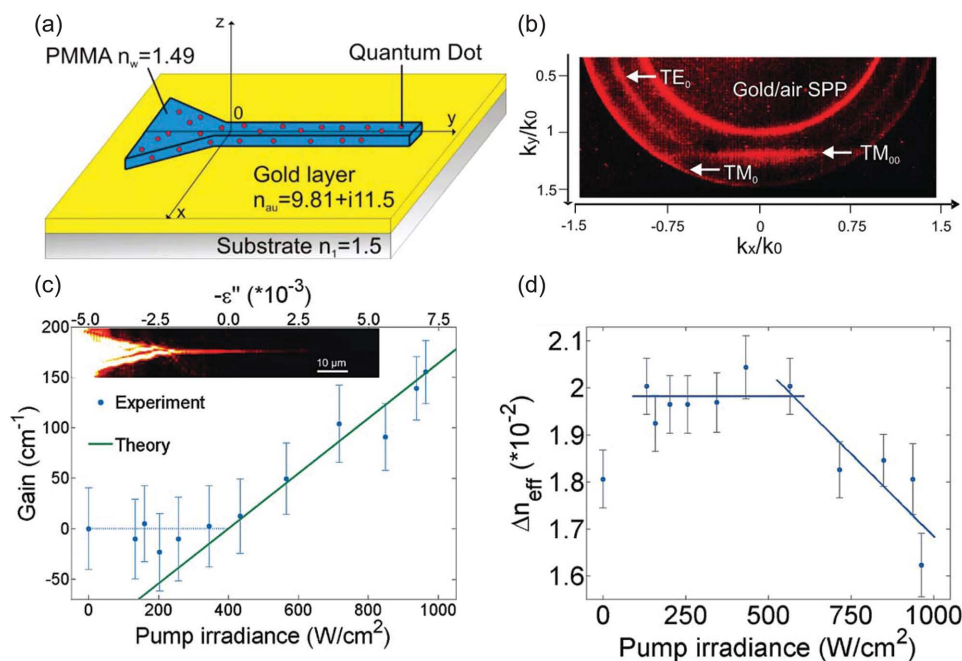

Figure 19. a) Schematic of a DLSPP waveguide with the PMMA core doped with quantum dots (QDs). b) QD fluorescence near $\lambda = 1500$ nm recorded in the Fourier plane under the optical excitation ($\lambda = 532$ nm). The arrows indicate the different effective indices ($n_{eff} = k_y/k_0$) of the modes existing within the illuminated area. c) The intensity dependence of modal gain. Inset shows the LMR image of taper-assisted launching of the DLSPPW mode and its propagation along the waveguide. d) The intensity dependence of the full-width-at-half-maximum (FWHM) of the effective mode index variation Δn_{eff} related to the mode propagation length. Reproduced with permission.[169] Copyright 2009, American Chemical Society.
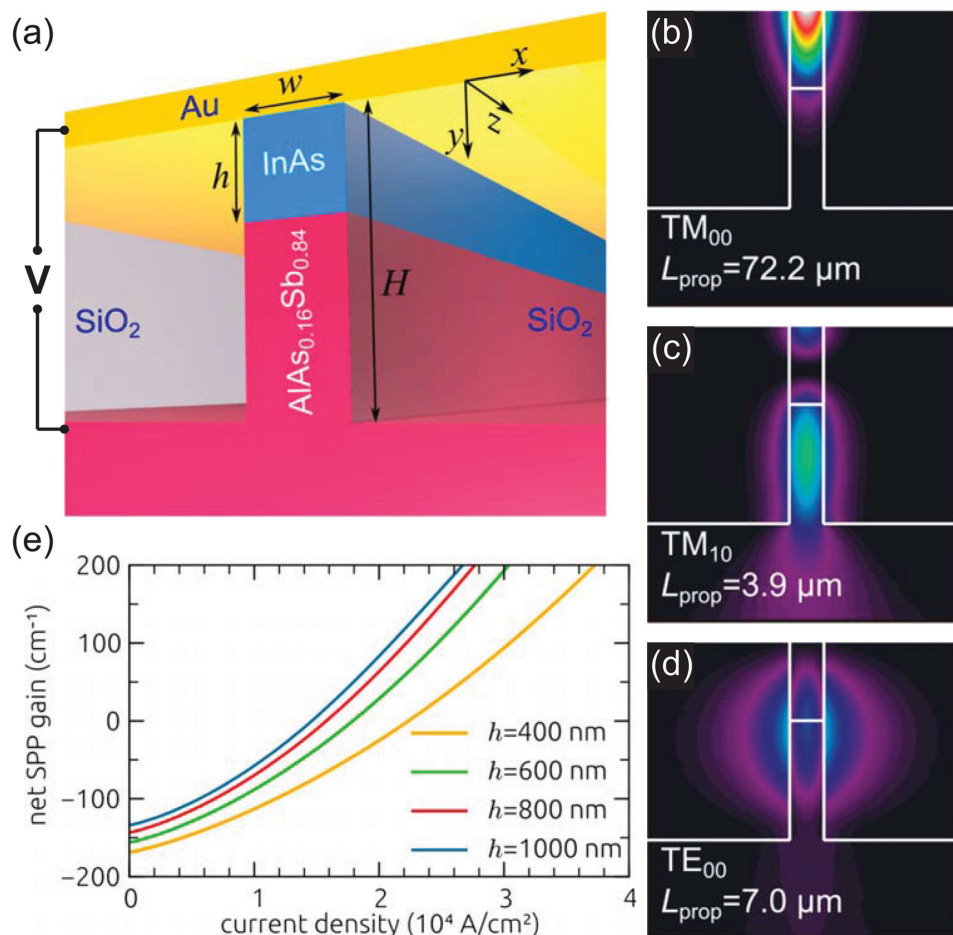
Figure 20. a) Schematics of an active plasmonic waveguide based on the active p-type InAs ridge and the passive p-type AlAs$_{0.16}$Sb$_{0.84}$ layer. b–d) Power flow distributions of the TM$_{00}$ guided as well as TM$_{10}$ and TE$_{00}$ leaky SPP modes for the waveguide with w = 350 nm, H = 2000 nm, and h = 800 nm at the SPP wavelength of λ = 3.16 μm, which corresponds to the maximum gain in InAs. e) Current-gain characteristic for the TM$_{00}$ mode for different sizes of the active region. Adapted with permission.[54] Copyright 2012, ACS.

with the effective index (n_{eff} = 2.68) and the propagation length of L_{prop} = 72.2 μm (Figure 20b–d).

Upon application of a bias voltage, electrons and holes are injected in the active InAs region, creating the population inversion (Figure 20a). When the energy separation between the quasi-Fermi levels of electrons and holes becomes equal to energy of the SPP, stimulated emission into the SPP mode is initiated. The SPP mode propagation losses can be fully compensated at moderate current densities ≈10–30 kA cm^{-2}; above these values the mode is efficiently amplified (Figure 20e). The possibility of the loss compensation for the SPP signal with 100 Gb s^{-1} bit-rate was demonstrated. This approach has been further developed to design a nanoscale plasmonic laser based on a SPP ring resonator.[165]

8. Other Types and Applications of DLSPP-Based Plasmonic Waveguides

8.1. Long-Range and Symmetric DLSPP Waveguides

The concept of long-range plasmonic modes can also be extended to the DLSPP waveguide geometry. It is based on

the fact that if the thickness of the SPP-supporting metal film becomes sufficiently small (few tens, typically, 20 nm), the SPP modes at its top and bottom interfaces become coupled.[172,173] Particularly interesting is the case of the film in a symmetric environment, when the dielectric above and below the metal film is the same material or different materials with very close refractive indexes. For the mode with a symmetric field distribution of the normal-to-the-surface component of the electric field, the electromagnetic field is pushed out of the metal, which leads to the dramatic reduction of the absorption losses with SPP propagation length of the symmetric mode on the centimeter scale. Its counterpart is a highly localized and very absorptive mode with an anti-symmetric field distribution. The metal film can be structured to achieve micrometer-wide metal stripe waveguides for a long-range SPP mode.[33]

This long-range propagation however comes at the price of an increased modal size and the effective index of the mode being closer to the refractive index of the surrounding media. The latter defines the lower limit for the waveguide bending radius to be of the order of several millimeters (see Table 2). To counteract these effects, an approach based on loading the long-range metal stripe waveguides with dielectric ridges was
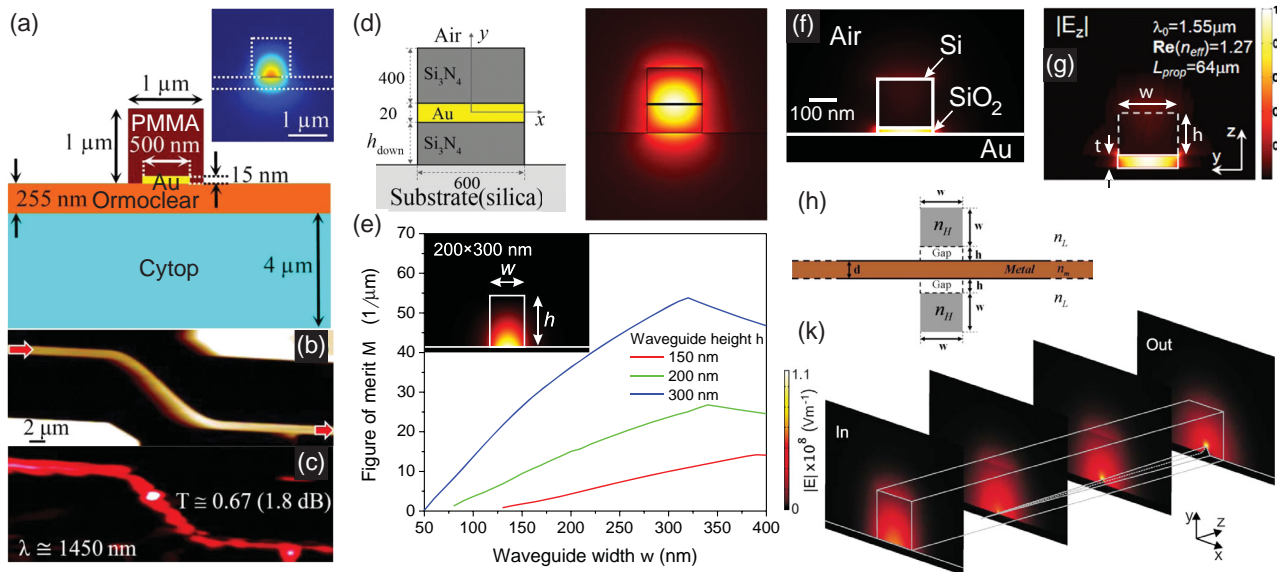
Figure 21. a) Schematic of the cross-section of the fabricated long-range DLSPP waveguide. The inset shows time-averaged electric field distribution of the fundamental LR-DLSPPW mode calculated at $\lambda = 1550$ nm. b) Topography and c) near-field optical images of a long-range DLSPPW S-bend at a wavelengths of $\lambda = 1450$ nm. Reproduced with permission.[176] Copyright 2011, Optical Society of America. d) Schematic of a symmetric DLSPP waveguide placed on a silica substrate and the electric field E_y distribution of the SPP mode in the optimized waveguide geometry ($h_{down} = 310$ nm). Reproduced with permission.[179] Copyright 2009, Optical Society of America. e) Figures of merit for Si/Al SPP waveguide. Inset shows the distribution of the power flow along the waveguide. Adapted with permission.[99] Copyright 2010, Optical Society of America. f) A hybrid optical waveguide based on a high refractive index nanowire separated from a metallic half-space by a nanoscale low refractive index dielectric spacer. g) DLSPPW-based realization of a hybrid waveguide: $|E_z|$ field profile and guiding characteristics of the mode in the case of $w = 200$ nm, $h = 150$ nm, and $t = 50$ nm. Reproduced with permission.[161] Copyright 2010, American Institute of Physics. h) Symmetric hybrid DLSPPW design. Reproduced with permission.[180] Copyright 2009, Optical Society of America. k) Adiabatic nanofocusing of the electromagnetic field in a hybrid DLSPPW–metal–ridge mode. Adapted with permission.[181] Copyright 2009, American Institute of Physics.

proposed[174,175] (**Figure 21**a): the dielectric ridge both localizes the mode and increases the effective index contrast. In order to obtain the longest propagation length, the key approach here is ensuring the most symmetric field distributions with respect to the metal stripe, corresponding to the minimal confinement of the plasmonic field in the metal and, therefore, minimizing absorption losses. This was realized by placing a high refractive index buffer layer between the metal film and a low refractive index substrate. Varying its thickness, waveguide width and height and the width of the gold stripe, the optimal waveguide geometries for various materials were found with the mode propagation lengths approaching several millimeters.[174,175] Well-defined propagation of the long-range DLSPPW mode with confinement approximately 1 μm and even below was observed at telecom wavelengths (Figures 21b,c).[176,177] The propagation length of the mode was about 0.5 mm (affected by the leakage due to a finite thickness of the dielectric layer and the fabrication imperfections), while the theoretical estimation for the potential propagation length is about 3 mm. An efficient transmission of the mode through a waveguide S-bend was demonstrated with just ≈1.8 dB loss for the waveguide separation of 10 μm and the S-bend horizontal length of 20 μm (Figure 21b,c).

An alternative development of the same idea is realized in the so-called symmetric DLSPP waveguides, where the dielectric core is mirrored across the thin metal film with an identical or similar ridge.[178,179] Symmetrization of the field profiles was achieved by varying the thickness of the bottom dielectric ridge

h_{down} (Figure 21d).[179] At the price of acceptable increase of the modal size, the propagation length can be increased up to 321 μm. More importantly, the strong guiding performance of the DLSPPW is preserved: the quality factors of the ring resonators made from the waveguide of such geometry are actually improved. They are even higher than those of micro-ring dielectric resonators, with plasmonic waveguides having an additional advantage to efficiently control the mode utilizing the metallic layer for active functions.

8.2. Semiconductor-loaded Waveguides

As discussed above, one of the crucial advantages of the plasmonic approach is its seamless integration into electronic microchips to realize hybrid electronic/photonic circuits where electronic and photonic signals can be transferred along the same lines. Furthermore, with the possibility of their interaction through electro-optic or thermo-optic effects, active control nodes can be introduced, making the circuitry fully functional. In order to achieve such integration in the case of DLSPP waveguides, their material platform should be compatible with the CMOS fabrication processes used in microelectronics. Silicon in this case becomes one of the main candidates for the dielectric core material. An additional advantage of using high refractive index material is the possibility of higher confinement of the plasmonic mode, providing also an increase of the mode effective index. This makes the DLSPPW components more compact, allowing higher integration density.

ADVANCED
OPTICAL
MATERIALS
www.advopticalmat.de

Materials
Views
www.MaterialsViews.com

REVIEW

Comprehensive numerical analysis of Si-based DLSPP waveguides can be realized in conjunction with the CMOS-compatible aluminum or copper material platform.[99] As expected, with the DLSPPW design scaled down in 2–3 times, a substantial decrease of the mode area (≈5–10 times) was observed accompanied by a proportional decrease of the propagation length (below 10 μm). The performance of Si-based waveguides depends on their width–height ratio. The dependence of a 'local' figure of merit (Equation (12) with additional assumptions on the fabrication resolution) on the geometrical parameters of the Si/Al waveguide is presented in Figure 21e, implying the cross-section 300 nm × 300 nm to be close to the optimal. Additionally, the performance of CMOS-compatible Al- and Cu-based Si-DLSPP waveguides was compared with that of the conventional Si-DLSPPW design utilizing gold. Aluminium showed the plasmonic guiding properties as good as those of gold, while for copper the propagation lengths were found to be ≈2 times shorter. As was demonstrated later, the plasmonic properties of copper deposited in a standard CMOS fabrication process may match those of the noble metals, thus improving the FOM.[182,183] DLSPP waveguides based on CdS nanostripe deposited on an Ag film were also demonstrated in visible frequencies.[184]

8.3. Hybrid DLSPP Waveguides

An interesting approach to the plasmonic mode confinement in DLSPPW-type waveguides relies on a stripe made of high refractive index material placed at nanometer distance above a metal surface using a low refractive index spacer (Figure 21f).[185] Plasmonic oscillations at the metal interface of the resulting gap produce the polarization charges at the stripe interface of the gap, efficiently screening the electromagnetic field penetration into the stripe. This results in a highly localized plasmonic mode. In some sense, the nature of the mode here is similar to the one in MIM plasmonic waveguides. In alternative consideration, the enhancement of the field can be regarded as a result of continuity condition for the electric displacement, resulting in stronger fields in the low refractive index gap. The term 'hybrid' comes from the fact that the origin of the mode can be traced to the coupling of a 2D plasmonic wave at the metal interface with a photonic mode in the high refractive index core.[185]

This approach was first developed for a silicon dielectric core separated from a silver surface by a 50 nm silica providing strong confinement of the mode in the silica gap (Figure 21g).[161,186,187] Such waveguides show smaller cross-talk in comparison with the conventional plasmonic DLSPPW design, allowing a 1.5 μm center-to-center integration level without noticeable signal transfer. The theoretical propagation length of the mode was found to be 64 μm for silver[188] while for gold[189] it is reduced to approximately 15 μm. Component integration level on the other hand offers a promise to be at a 1 μm level: the mode transmission of ≈70% was measured through both a circular bend[161] and a splitter of this size[186] and a coupler to conventional silicon waveguiding circuitry was demonstrated.[190] The wavelength-selective components such as WRRs and add-drop filters of 2 μm radius were also

demonstrated,[187] and it seems feasible that their size can be further reduced. The advantage of the hybrid approach is a larger propagation length with approximately the same effective mode index and mode size.[191] An alternative design of the hybrid Si-plasmonic waveguide uses a void along an axis of a Si ridge.[192]

Combining the hybrid-DLSPPW approach with the idea of increasing the mode propagation length using symmetric distribution of the SPP mode in a thin metal film geometry (discussed in the previous section), symmetric hybrid-DLSPP waveguides were proposed (Figure 21h).[180,193] With the optimal geometrical parameters of such waveguides, the propagation length can be increased to almost 1 mm level at a cost of a cross-talk defined integration level of 3–3.5 μm. On the other hand, using metal instead of high-index dielectric material (which implements a MIM-type guiding principle in the so-called metal-loaded SPP waveguides) allows extremely high mode confinement levels and strong guiding properties (integration level of 65 nm, electronic circuit scales waveguide bending with a vanishing bending radius), as usual, at the price of the increased attenuation $L_{prop} \approx 0.5$ μm (see Table 2).[69] The implementation of active, e.g., III–V, semiconductor materials for the waveguide core has a crucial advantage for the realization of the amplification of the guided mode in this geometry.[54,52] Finally, it should be noted that graphene-based DLSPPW waveguides have been recently proposed, promising electrically-controlled active functionalities and enhanced non-linear properties in mid- to far-infrared regions.[194,195]

8.4. Other Applications of DLSPPWs

We finally briefly overview other functionalities and applications offered by the DLSPPW approach. The portfolio of DLSPPW passive, wavelength-selective and active components was further extended with experimental demonstration of an integrated power monitor. Propagating along a straight waveguide section, the DLSPPW mode inevitably experiences absorption, which leads to a temperature change in the metal film supporting the waveguide. This results in a change of the film resistance, which can be monitored by a carefully balanced electrical scheme (Wheatstone bridge).[196] The waveguide section of a 46 μm length provides approximately 1.8 μV μW^{-1} sensitivity having only a weak dependence on the signal wavelength with a bandwidth up to 550 Hz in modulation frequencies. The SPP signal power as low as fractions of microwatts can be detected.

As discussed above, the transmission through the DLSPPW ring resonator is highly sensitive to the phase delay acquired by the mode during a cycle around the ring, which in its turn is defined by the refractive index of the ring material. In case of polymers, the refractive index is temperature-dependent and can be changed through a resistive heating of the underlying metal film. This was used to realize DLSPPW thermo-optic components. Looking from another prospective, this means that the WRR transmission is sensitive to the ambient temperature, leading to the idea of a WRR-based temperature sensor.[197,198] The temperature variations of about ≈1 °C were monitored with the estimation of a minimal detectable level

www.MaterialsViews.com

ADVANCED
OPTICAL
MATERIALS
www.advopticalmat.de

REVIEW

of 10^{-2} °C. The component size of ≈10 μm makes it specifically suitable for local temperature detection, furthermore by design being easily integrated into an on-chip architecture.

The idea of adiabatic field compression was used to develop a triangular DLSPPW profiles for nanofocusing of the supported SPP modes; the focusing down to a 100 nm spot was demonstrated.[199] Similarly, nanofocusing to truly nanoscale dimensions was reported by incorporation into the dielectric core of DLSPPW a triangular metallic ridge waveguide with an adiabatically increasing height (Figure 21k).[181] Through adiabatic transformation of the DLSPPW mode, a dramatic concentration of the SPP field at the ridge tip can be achieved in an approximately 11 nm × 5 nm area. This focused mode can be impedance matched to a neighboring material to provide effective light absorption in a 30 nm × 30 nm area in the near field of the waveguide tip. Such local effects are highly demanded for the development of high-density data storage, and in particular for heat-assisted magnetic recording.[200] Alternative applications of this phenomenon include sensing, scanning near-field microscopy and the realization of nanoscale light sources.

It is hardly possible to give an exhaustive list of DLSPPW applications. Concluding this section, we will just highlight the DLSPPW-related approaches in refractive index sensing for bio-[201,202] and chemical sensing,[203,204] for studies of quantum properties of plasmons[205–207] and their Anderson localization.[208]

9. Conclusions

Plasmonics offers a unique opportunity to introduce light into the nanoworld. Breaking the diffraction limit of light, the plasmonic approach makes a qualitative step into a new spatial domain, where optics can now play an important and promising role. From the practical point of view, plasmonics offers a vast family of applications in the various fields from biology and sensing to metamaterials and quantum technologies. We focused here only on applications of plasmonics in highly-integrated fully-functional optical circuits which can match the integration level of their electronic counterparts and are easily integratable into them to produce new generation of hybrid electronic/photonic devices. We overviewed the recent advances in the development of active and passive components for such circuits on the basis of dielectric-loaded plasmonic waveguides. The DLSPPW approach provides subwavelength confinement of the plasmonic mode along with the micrometer level of photonic integration, allowing experimentally proven WDM data transmission rates of up to 0.5 Tb s^{-1}, while the theoretical limit is on the order of 10 Tb s^{-1} in a single data stream, if nonlinearities are neglected. A complete toolbox of passive and wavelength-selective components including bends, splitters, Bragg reflectors, ring resonators, etc. has been demonstrated. Furthermore, all-optical, electro-optical and thermo-optical components have been developed for active functionalities. The DLSPPW approach provides vast opportunities for the development of other improved and purpose-fit plasmonic waveguide designs as well as has a potential for a number of alternative applications. Such waveguides can be incorporated in other photonic networks based, e.g., on Si photonics to provide low-energy,

high-speed active components, which can be realized engineering strong light–matter interaction in plasmonic devices.

[1] Optical Interconnects: The Silicon Approach (Eds: L. Pavesi, G. Guillot), Springer-Verlag, Berlin/Heidelberg, 2006.
[2] P. Bai, H. S. Chu, M. Gu, O. Kurniawan, E. Li, Phys. B 2010, 405, 2978.
[3] D. A. B Miller, Proc. IEEE 2009, 97, 1166.
[4] C. Koos, P. Vorreau, T. Vallaitis, P. Dumon, W. Bogaerts, R. Baets, B. Esembeson, I. Biaggio, T. Michinobu, F. Diederich, W. Freude, J. Leuthold, Nature Phot. 2009, 3, 216.
[5] T. Volz, A. Reinhard, M. Winger, A. Badolato, K. J. Hennessy, E. L. Hu, A. Imamoglu, Nature Phot. 2012, 6, 605.
[6] G. Shambat, B. Ellis, A. Majumdar, J. Petykiewicz, M. A. Mayer, T. Sarmiento, J. Harris, E. E. Haller, J. Vuckovic, Nature Commun. 2011, 2, 539.
[7] Plasmonic Nanoguides and Circuits (Ed: S. I. Bozhevolnyi), Pan Stanford Publishing, Singapore, 2009.
[8] H. Raether, Surface Plasmon on Smooth and Rough Surfaces and on Gratings, Springer-Verlag, Berlin, Germany 1988.
[9] S. A. Maier, Plasmonics: Fundamentals and Applications, Springer, New York, USA 2007.
[10] M. Quinten, Optical Properties of Nanoparticle systems, Wiley-VCH, Weinheim, Germany 2011.
[11] J. Nelayah, M. Kociak, O. Stephan, F. J. Garcia de Abaho, M. Tence, L. Henrard, D. Taverna, I. Pastoriza-Santos, L. M. Liz-Marzan, C. Colliex, Nature Phys. 2007, 3, 348.
[12] J. A. Scholl, A. L. Koh, J. A. Dionne, Nature 2012, 483, 421.
[13] A. V. Zayats, I. I. Smolyaninov, A. A. Maradudin, Phys. Rep. 2005, 408, 131.
[14] J. A. Schuller, E. S. Barnard, W. Cai, Y. C. Jun, J. S. White, M L. Brongersma, Nature Mater. 2010, 9, 193.
[15] S. Kawata, Y. Inouye, P. Verma, Nature Photon. 2009, 3, 388.
[16] N. Liu, M. L. Tang, M. Hentschel, H. Giessen, A. P. Alivisatos, Nature Mater. 2011, 10, 631.
[17] C. Novo, A. M. Funston, P. Mulvaney, Nature Mater. 2008, 3, 598.
[18] J. N. Anker, W. P. Hall, O. Lyandres, N. C. Shah, J. Zhao, R. P. Van Duyne, Nature Mater. 2008, 7, 442.
[19] A. V. Kabashin, P. Evans, S. Pastkovsky, W. Hendren, G. A. Wurtz, R. Atkinson, R. Pollard, V. A. Podolskiy, A. V. Zayats, Nature Mater. 2009, 8, 867.
[20] K. Kneipp, Y. Wang, H. Kneipp, L. T. Perelman, I. Itzkan, R. R. Dasari, M. S. Feld, Phys. Rev. Lett. 1997, 78, 1667.
[21] S. Nie, S. R. Emory, Science 1997, 275, 1102.
[22] M. Kauranen, A. V. Zayats, Nature Photon. 2012, 6, 737.
[23] P. Ginzburg, A. V. Krasavin, G. A. Wurtz, A. V. Zayats, ACS Photonics 2015, 2, 8.
[24] W. Dickson, G. A. Wurtz, P. Evans, D. O'Connor, R. Atkinson, R. Pollard, A. V. Zayats, Phys. Rev. B 2007, 76, 115411.
[25] G. A. Wurtz, R. Pollard, W. Hendren, G. P. Wiederrecht, D. J. Gosztola, V. A. Podolskiy, A. V. Zayats, Nature Nanotechnol. 2011, 6, 107.

[26] M. Ren, B. Jia, J.-Y. Ou, E. Plum, J. Zhang, K. F. MacDonald, A. E. Nikolaenko, J. Xu, M. Gu, N. I. Zheludev, *Adv. Mater.* **2011**, *23*, 5540.

[27] A. D. Neira, N. Olivier, M. E. Nasir, W. Dickson, G. A. Wurtz, A. V. Zayats, *Nat. Commun.* **2015**, *6*, 7757.

[28] Y. Pu, R. Grange, C.-L. Hsieh, D. Psaltis, *Phys. Rev. Lett.* **2010**, *104*, 207402.

[29] P. Ginzburg, A. Krasavin, Y. Sonnefraud, A. Murphy, R. J. Pollard, S. A. Maier, A. V. Zayats, *Phys. Rev. B* **2012**, *86*, 085422.

[30] P. Genevet, J. Tetienne, E. Gatzogiannis, R. Blanchard, M. A. Kats, M. O. Scully, F. Capasso, *Nano. Lett.* **2010**, *10*, 4880.

[31] P. Ginzburg, A. V. Krasavin, A. V. Zayats, *New J. Phys.* **2013**, *15*, 013031.

[32] M. L. Brongersma, V. M. Shalaev, *Science* **2010**, *23*, 440.

[33] J. Jiang, C. L. Callender, S. Jacob, J. P. Noad, S. Chen, J. Ballato, D. W. SmithJr., *Appl. Opt.* **2008**, *47*, 3892.

[34] A. V. Krasavin, A. V. Zayats, *Opt. Lett.* **2010**, *35*, 2118.

[35] S. I. Bozhevolnyi, V. S. Volkov, E. Devaux, J.-Y. Laluet, T. W. Ebbesen, *Nature* **2006**, *440*, 508.

[36] L. Liu, Z. Han, S. He, *Opt. Express* **2005**, *13*, 6645.

[37] H. T. Miyazaki, Y. Kurokawa*Phys. Rev. Lett.* **2006**, *96*, 097401.

[38] J. Takahara, S. Yamagishi, H. Taki, A. Morimoto, T. Kobayashi, *Opt. Lett.* **1997**, *22*, 475.

[39] J. E. Verhagen, M. Spasenovic, A. Polman, L. (Kobus) Kuipers, *Phys. Rev. Lett.* **2009**, *102*, 203904.

[40] A. V. Krasavin, A. V. Zayats, *Opt. Lett.* **2011**, *36*, 3127.

[41] S. A. Maier, M. L. Brongersma, P. G. Kik, S. Meltzer, A. A. G. Requicha, H. A. Atwater, *Adv. Mater.* **2001**, *13*, 1501.

[42] V. J. Sorger, Z. Ye, R. F. Oulton, Y. Wang, G. Bartal, X. Yin, X. Zhang, *Nature Commun.* **2011**, *2*, 331.

[43] H. Hu, D. Ji, X. Zeng, K. Liu, Q. Gan, *Sci. Rep.* **2012**, *3*, 1249.

[44] N. Vasilantonakis, M. E. Nasir, W. Dickson, G. A. Wurtz, A. V. Zayats, *Laser Photonics Rev.* **2015**, *9*, 345.

[45] M. P. Nezhad, K. Tetz, Y. Fainman, *Opt. Express* **2004**, *12*, 4072.

[46] S. I. Bozhevolnyi, J. Jung, *Opt. Express* **2008**, *16*, 2676.

[47] J. Takahara, T. Kobayashi, *Opt. Photonics News* **2004**, *October*, 54.

[48] S. A. Maier, P. G. Kik, H. A. Atwater, *Phys. Rev. B* **2003**, *67*, 205402.

[49] I. De Leon, P. Berini, *Phys. Rev. B* **2008**, *78*, 161401(R).

[50] I. P. Radko, M. G. Nielsen, O. Albrektsen, S. I. Bozhevolnyi, *Opt. Express* **2010**, *18*, 18633.

[51] I. De Leon, P. Berini, *Nature Phot.* **2010**, *4*, 382.

[52] R. F. Oulton, V. J. Sorger, T. Zentgraf, R.-M. Ma, C. Gladden, L. Dai, G. Bartal, X. Zhang, *Nature* **2009**, *461*, 629.

[53] A. V. Krasavin, T. P. Vo, W. Dickson, P. M. Bolger, A. V. Zayats, *Nano Lett.* **2011**, *11*, 2235.

[54] D. Yu. Fedyanin, A. V. Krasavin, A. V. Arsenin, A. V. Zayats, *Nano Lett.* **2012**, *12*, 2459.

[55] M. Khajavikhan, A. Simic, M. Katz, J. H. Lee1, B. Slutsky, A. Mizrahi1, V. Lomakin, Y. Fainman, *Nature* **2012**, *482*, 204.

[56] R.-M. Ma, R. F. Oulton, V. J. Sorger, G. Bartal, X. Zhang, *Nature Mater.* **2011**, *10*, 110.

[57] M. A. Noginov, G. Zhu, A. M. Belgrave, R. Bakker, V. M. Shalaev, E. E. Narimanov, S. Stout, E. Herz, T. Suteewong, U. Wiesner, *Nature* **2009**, *460*, 1110.

[58] S.-H. Kwon, J.-H. Kang, C. Seassal, S.-K. Kim, P. Regreny, Y.-H. Lee, C. M. Lieber, H.-G. Park, *Nano Lett.* **2010**, *10*, 3679.

[59] M. T. Hill, M. Marell, E. S. P. Leong, B. Smalbrugge, Y. Zhu, M. Sun, P. J. van Veldhoven, E. Jan Geluk, F. Karouta, Y.-S. Oei, R. Nötzel, C.-Z. Ning, M. K. Smit, *Opt. Express* **2009**, *17*, 11107.

[60] G. W. Ford, W. H. Weber, *Phys. Rep.* **1984**, *113*, 195.

[61] P. M. Bolger, W. Dickson, A. V. Krasavin, L. Liebscher, S. G. Hickey, D. V. Skryabin, A. V. Zayats, *Opt. Lett.* **2010**, *35*, 1197.

[62] K. Liu, C. R. Ye, S. Khan, V. J. Sorger, *Laser Photon. Rev.* **2015**, *9*, 172.

[63] D. Pacifici, H. J. Lezec, H. A. Atwater, *Nature Phot.* **2007**, *1*, 402.

[64] R. A. Pala, K. T. Shimizu, N. A. Melosh, M. L. Brongersma, *Nano Lett.* **2008**, *8*, 1506.

[65] M. J. Dicken, L. A. Sweatlock, D. Pacifici, H. J. Lezec, K. Bhattacharya, H. A. Atwater, *Nano Lett.* **2008**, *8*, 4048.

[66] J. A. Dionne, K. Diest, L. A. Sweatlock, H. A. Atwater, *Nano Lett.* **2009**, *9*, 897.

[67] A. Melikyan, N. Lindenmann, S. Walheim, P. M. Leufke, S. Ulrich, J. Ye, P. Vincze, H. Hahn, Th. Schimmel, C. Koos, W. Freude, J. Leuthold, *Opt. Express* **2011**, *19*, 8855.

[68] A. Melikyan, L. Alloatti, A. Muslija, D. Hillerkuss, P. C. Schindler, J. Li, R. Palmer, D. Korn, S. Muehlbrandt, D. Van Thourhout, B. Chen, R. Dinu, M. Sommer, C. Koos, M. Kohl, W. Freude, J. Leuthold, *Nature Photon.* **2014**, *8*, 229.

[69] A. V. Krasavin, A. V. Zayats, *Phys. Rev. Lett.* **2012**, *109*, 053901.

[70] K. F. MacDonald, Z. L. Samson, M. I. Stockman, N. I. Zheludev, *Nature Phot.* **2008**, *3*, 55.

[71] A. V. Akimov, A. Mukherjee, C. L. Yu, D. E. Chang, A. S. Zibrov, P. R. Hemmer, H. Park, M. D. Lukin, *Nature* **2007**, *450*, 402.

[72] K. C. Y. Huang, M.-K. Seo, T. Sarmiento, Y. Huo, J. S. Harris, M. L. Brongersma, *Nature Phot.* **2014**, *8*, 244.

[73] D. M. Koller, A. Hohenau, H. Ditlbacher, N. Galler, F. Reil, F. R. Aussenegg, A. Leitner, E. J. W. List, J. R. Krenn, *Nature Phot.* **2008**, *2*, 684.

[74] Y.-S. No, J.-H. Choi, H.-S. Ee, M.-S. Hwang, K.-Y. Jeong, E.-K. Lee, M.-K. Seo, S.-H. Kwon, H.-G. Park, *Nano Lett.* **2013**, *13*, 772.

[75] H. Ditlbacher, F. R. Aussenegg, J. R. Krenn, B. Lamprecht, G. Jakopic, G. Leising, *Appl. Phys. Lett.* **2006**, *89*, 161101.

[76] A. Akbari, R. N. Tait, P. Berini, *Opt. Express* **2010**, *18*, 8505.

[77] D.-S. Ly-Gagnon, K. C. Balram, J. S. White, P. Wahl, M. L. Brongersma, D. A.B. Miller, *Nanophotonics* **2012**, *1*, 9.

[78] A. Kumar, J. Gosciniak, V. S. Volkov, S. Papaioannou, D. Kalavrouziotis, K. Vyrsokinos, J.-C. Weeber, K. Hassan, L. Markey, A. Dereux, T. Tekin, M. Waldow, D. Apostolopoulos, H. Avramopoulos, N. Pleros, S. I. Bozhevolnyi, *Laser Photonics Rev.* **2013**, *6*, 938.

[79] T. Holmgaard, S. I. Bozhevolnyi, L. Markey, A. Dereux, *Appl. Phys. Lett.* **2008**, *92*, 011124.

[80] C. Reinhardt, S. Passinger, B. Chichkov, C. Marquart, I. Radko, S. Bozhevolnyi, *Opt. Lett.* **2006**, *31*, 1307.

[81] C. Reinhardt, A. Seidel, A. Evlyukhin, ·W. Cheng, R. Kiyan, B. Chichkov, *Appl. Phys. A* **2010**, *100*, 347.

[82] H. Luo, Y. Li, H.-B. Cui, H. Yang, Q.-H. Gong, *Appl. Phys. A* **2009**, *97*, 709.

[83] A. Seidel, C. Ohrt, S. Passinger, C. Reinhardt, R. Kiyan, B. N. Chichkov, *J. Opt. Soc. Am. B: Opt. Phys* **2009**, *26*, 810.

[84] S. Massenot, J. Grandidier, A. Bouhelier, G. Colas des Francs, L. Markey, J.-C. Weeber, A. Dereux, J. Renger, M. U. Gonzàlez, R. Quidant, *Appl. Phys. Lett.* **2007**, *91*, 243102.

[85] Q. Li, W. Zhang, H. Zhao, M. Qiu, *J. Lightwave Technol.* **2013**, *31*, 4051.

[86] A. V. Krasavin, A. V. Zayats, *Phys. Rev. B* **2008**, *78*, 045425.

[87] H. Subbaraman, X. Xu, A. Hosseini, X. Zhang, Y. Zhang, D. Kwong, R. T. Chen, *Opt. Express* **2015**, *23*, 2487.

[88] G. T. Reed, G. Mashanovich, F. Y. Gardes, D. J. Thomson, *Nature Photon.* **2010**, *4*, 518.

[89] S. Papaioannou, G. Giannoulis, K. Vyrsokinos, F. Leroy, F. Zacharatos, L. Markey, J.-C. Weeber, A. Dereux, S. I. Bozhevolnyi, A. Prinzen, D. Apostolopoulos, H. Avramopoulos, N. Pleros, *IEEE Photon. Technol. Lett.* **2015**, *27*, 963.

[90] N. C. Harris, Y. Ma, J. Mower, T. Baehr-Jones, D. Englund, M. Hochberg, C. Galland, *Opt. Express* **2014**, *22*, 10487.

[91] D. M. Beggs, T. P. White, L. Cairns, L. O'Faolain, T. F. Krauss, *IEEE Photon. Technol. Lett.* **2009**, *21*, 24.

[92] Y. Cui, K. Liu, D. L. MacFarlane, J.-B. Lee, *Opt. Lett.* **2010**, *35*, 3613.

[93] P. Dong, S. Liao, H. Liang, R. Shafiiha, D. Feng, G. Li, X. Zheng, A. V. Krishnamoorthy, M. Asghari, *Opt. Express* **2010**, *18*, 25225.

[94] M. Yang, W. M. J. Green, S. Assefa, J. Van Campenhout, B. G. Lee, C. V. Jahnes, F. E. Doany, C. L. Schow, J. A. Kash, Y. A. Vlasov, *Opt. Express* **2010**, *19*, 47.

[95] K. Hassan, J.-C. Weeber, L. Markey, A. Dereux, *J. Appl. Phys.* **2011**, *110*, 023106.

[96] Q. Xu, B. Schmidt, S. Pradhan, M. Lipson, *Nature* **2005**, *435*, 325.

[97] A. Hosseini, X. Xu, H. Subbaraman, C.-Y. Lin, S. Rahimi, R. T. Chen, *Opt. Express* **2012**, *20*, 12318.

[98] T. Holmgaard, S. I. Bozhevolnyi, *Phys. Rev. B* **2007**, *75*, 245405.

[99] A. V. Krasavin, A. V. Zayats, *Opt. Express* **2010**, *18*, 11791.

[100] A. Hosseini, A. Nieuwoudt, Y. Massoud, *IEEE Photon. Technol. Lett.* **2007**, *19*, 522.

[101] J. Grandidier, S. Massenot, G. Colas des Francs, A. Bouhelier, J.-C. Weeber, L. Markey, A. Dereux, *Phys. Rev. B* **2008**, *78*, 245419.

[102] J. Jung, *J. Opt. Soc. Korea* **2010**, *14*, 277.

[103] H. Zhao, Y. Li, G. Zhang, *Opt. Comm.* **2012**, *285*, 1091.

[104] I. P. Radko, J. Fiutowski, L. Tavares, H.-G. Rubahn, S. I. Bozhevolnyi, *Opt. Express* **2011**, *19*, 15155.

[105] T. Leißner, C. Lemke, J. Fiutowski, J. W. Radke, A. Klick, L. Tavares, J. Kjelstrup-Hansen, H.-G. Rubahn, M. Bauer, *Phys. Rev. Lett.* **2013**, *111*, 046802.

[106] Y. Li, H. Zhao, A. Ma, X. Zhang, *Opt. Comm.* **2011**, *284*, 2839.

[107] B. Steinberger, A. Hohenau, H. Ditlbacher, A. L. Stepanov, A. Drezet, F. R. Aussenegg, A. Leitner, J. R. Krenn, *Appl. Phys. Lett.* **2006**, *88*, 094104.

[108] T. Holmgaard, S. I. Bozhevolnyi, L. Markey, A. Dereux, A. V. Krasavin, P. Bolger, A. V. Zayats, *Phys. Rev. B* **2008**, *78*, 165431.

[109] A. V. Krasavin, A. V. Zayats, *Appl. Phys. Lett.* **2007**, *90*, 211101.

[110] A. Krishnan, C. J. Regan, L. Grave de Peralta, A. A. Bernussi, *Appl. Phys. Lett.* **2010**, *97*, 231110.

[111] T. Holmgaard, Z. Chen, S. I. Bozhevolnyi, L. Markey, A. Dereux, *J. Lightwave Technol.* **2009**, *27*, 5521.

[112] B. Steinberger, A. Hohenau, H. Ditlbacher, F. R. Aussenegg, A. Leitner, J. R. Krenn, *Appl. Phys. Lett.* **2007**, *91*, 081111.

[113] S. J. Orfanidis, *Electromagnetic Waves and Antennas*, Rutgers University, USA **2008**.

[114] G. Giannoulis, D. Kalavrouziotis, D. Apostolopoulos, S. Papaioannou, A. Kumar, S. Bozhevolnyi, L. Markey, K. Hassan, J.-C. Weeber, A. Dereux, M. Baus, M. Karl, T. Tekin, O. Tsilipakos, A. K. Pitilakis, E. E. Kriezis, K. Vyrsokinos, H. Avramopoulos, N. Pleros, *IEEE Phot. Technol. Lett.* **2012**, *24*, 374.

[115] D. Kalavrouziotis, S. Papaioannou, G. Giannoulis, D. Apostolopoulos, K. Hassan, L. Markey, J.-C. Weeber, A. Dereux, A. Kumar, S. I. Bozhevolnyi, M. Baus, M. Karl, T. Tekin, O. Tsilipakos, A. Pitilakis, E. E. Kriezis, H. Avramopoulos, K. Vyrsokinos, N. Pleros, *Opt. Express* **2012**, *20*, 7655.

[116] T. Holmgaard, Z. Chen, S. I. Bozhevolnyi, L. Markey, A. Dereux, A. V. Krasavin, A. V. Zayats, *Opt. Express.* **2008**, *16*, 13585.

[117] M. G. Nielsen, J.-C. Weeber, K. Hassan, J. Fatome, C. Finot, S. Kaya, L. Markey, O. Albrektsen, S. I. Bozhevolnyi, G. Millot, A. Dereux, *J. Lightwave Technol.* **2012**, *30*, 3118.

[118] D. G. Zhang, X.-C. Yuan, A. Bouhelier, P. Wang, H. Ming, *Opt. Lett.* **2010**, *35*, 408.

[119] S.-Y. Hsu, T.-H. Jen, E.-H. Lin, P.-K. Wei, *Plasmonics* **2011**, *6*, 557.

[120] O. Tsilipakos, A. Pitilakis, T. V. Yioultsis, S. Papaioannou, K. Vyrsokinos, D. Kalavrouziotis, G. Giannoulis, D. Apostolopoulos, H. Avramopoulos, T. Tekin, M. Baus, M. Karl, K. Hassan, J.-C. Weeber, L. Markey, A. Dereux, A. Kumar, S. I. Bozhevolnyi, N. Pleros, E. E. Kriezis, *IEEE J. Quantum Electron.* **2012**, *48*, 678.

[121] S. I. P. Radko, S. I. Bozhevolnyi, G. Brucoli, L. Martin-Moreno, F. J. Garcia-Vidal, A. Boltasseva, *Opt. Express* **2009**, *17*, 7228.

[122] S. Randhawa, M. U. González, J. Renger, S. Enoch, R. Quidant, *Opt. Express* **2010**, *18*, 14496.

[123] X. Li, L. Huang, Q. Tan, B. Bai, G. Jin, *Opt. Express* **2011**, *19*, 6541.

[124] J. Gosciniak, V. S. Volkov, S. I. Bozhevolnyi, L. Markey, S. Massenot, A. Dereux, *Opt. Express* **2010**, *18*, 5314.

[125] R. M. Briggs, J. Grandidier, S. P. Burgos, E. Feigenbaum, H. A. Atwater, *Nano Lett.* **2010**, *10*, 4851.

[126] Z. Han, I. P. Radko, N. Mazurski, B. Desiatov, J. Beermann, O. Albrektsen, U. Levy, S. I. Bozhevolnyi, *Nano Lett.* **2015**, *15*, 476.

[127] S. Yue, Z. Li, J.-J. Chen, Q.-H. Gong, *Chin. Phys. Lett.* **2010**, *27*, 027303.

[128] G. Yuan, P. Wang, Y. Lu, H. Ming, *Opt. Express* **2009**, *17*, 12594.

[129] S. Passinger, A. Seidel, C. Ohrt, C. Reinhardt, A. Stepanov, R. Kiyan, B. N. Chichkov, *Opt. Express* **2008**, *16*, 14369.

[130] Z. Zhu, C. E. Garcia-Ortiz, Z. Han, I. P. Radko, S. I. Bozhevolnyi, *Appl. Phys. Lett.* **2013**, *103*, 061108.

[131] R. Kashyap, *Fiber Bragg Gratings*, Academic Press, San Diego, USA, **1999**.

[132] T. Holmgaard, Z. Chen, S. I. Bozhevolnyi, L. Markey, A. Dereux, A. V. Krasavin, A. V. Zayats, *Appl. Phys. Lett.* **2009**, *94*, 051111.

[133] T. Holmgaard, Z. Chen, S. I. Bozhevolnyi, L. Markey, A. Dereux, *Opt. Express* **2009**, *17*, 2968.

[134] M. A. Popovic, C. Manolatou, M. R. Watts, *Opt. Express* **2006**, *14*, 1208.

[135] C. Garcia, V. Coello, Z. Han, I. P. Radko, S. I. Bozhevolnyi, *Appl. Phys. B* **2012**, *107*, 401.

[136] S. Randhawa, A. V. Krasavin, T. Holmgaard, J. Renger, S. I. Bozhevolnyi, A. V. Zayats, R. Quidant, *Appl. Phys. Lett.* **2011**, *98*, 161102.

[137] O. Tsilipakos, E. E. Kriezis, *Opt. Comm.* **2010**, *283*, 3095.

[138] Z. Chen, T. Holmgaard, S. I. Bozhevolnyi, A. V. Krasavin, A. V. Zayats, L. Markey, A. Dereux, *Opt. Lett.* **2009**, *34*, 310.

[139] A. Boltasseva, S. I. Bozhevolnyi, *IEEE J. Sel. Top. Quantum Electron.* **2006**, *12*, 1233.

[140] A. V. Krasavin, N. I. Zheludev, *Appl. Phys. Lett.* **2004**, *84*, 1416.

[141] A V. Krasavin, A V. Zayats, N. I. Zheludev, *J. Opt. A* **2005**, *7*, S85.

[142] A. V. Krasavin, K. F. MacDonald, N. I. Zheludev, A. V. Zayats, *Appl. Phys. Lett.* **2004**, *85*, 3369.

[143] A. V. Krasavin, A. V. Zayats, *Opt. Comm.* **2010**, *283*, 1581.

[144] A. V. Krasavin, A. V. Zayats, *Appl. Phys. Lett.* **2010**, *97*, 041107.

[145] A. V. Krasavin, S. Randhawa, J.-S. Bouillard, J. Renger, R. Quidant, A. V. Zayats, *Opt. Express* **2011**, *19*, 25222.

[146] J.-C. Weeber, K. Hassan, L. Saviot, A. Dereux, C. Boissiere, O. Durupthy, C. Chaneac, E. Burov, A. Pastouret, *Opt. Express* **2012**, *20*, 27636.

[147] S. Randhawa, S. Lacheze, J. Renger, A. Bouhelier, R. Espiau de Lamaestre, A. Dereux, R. Quidant, *Opt. Express* **2012**, *20*, 2354.

[148] A. C. Tasolamprou, D. C. Zografopoulos, E. E. Kriezis, *J. Appl. Phys.* **2011**, *110*, 093102.

[149] D. A. B. Miller, *Opt. Express* **2012**, *20*, A293.

[150] C. Haffner, W. Heni, Y. Fedoryshyn, J. Niegemann, A. Melikyan, D. L. Elder, B. Baeuerle, Y. Salamin, A. Josten, U. Koch, C. Hoessbacher, F. Ducry, L. Juchli, A. Emboras, D. Hillerkuss, M. Kohl, L. R. Dalton, C. Hafner, J. Leuthold, *Nature Photon.* **2015**, *9*, 525.

[151] J. Gosciniak, S. I. Bozhevolnyi, T. B. Andersen, V. S. Volkov, J. Kjelstrup-Hansen, L. Markey, A. Dereux, *Opt. Express* **2010**, *12*, 1207.

[152] J. Gosciniak, L. Markey, A. Dereux, S. I. Bozhevolnyi, *Opt. Express* **2012**, *20*, 16300.

[153] J. Gosciniak, S. I. Bozhevolnyi, *Sci. Rep.* **2013**, *3*, 803.

[154] S. Papaioannou, K. Vyrsokinos, O. Tsilipakos, A. Pitilakis, K. Hassan, J.-C. Weeber, L. Markey, A. Dereux, S. I. Bozhevolnyi, A. Miliou, E. E. Kriezis, N. Pleros, *J. Lightwave Technol.* **2011**, *29*, 3185.

[155] S. Papaioannou, D. Kalavrouziotis, K. Vyrsokinos, J.-C. Weeber, K. Hassan, L. Markey, A. Dereux, A. Kumar, S. I. Bozhevolnyi,

M. Baus, T. Tekin, D. Apostolopoulos, H. Avramopoulos, N. Pleros, *Sci. Rep.* **2012**, *2*, 652.

[156] D. Kalavrouziotis, S. Papaioannou, K. Vyrsokinos, A. Kumar, S. I. Bozhevolnyi, K. Hassan, L. Markey, J.-C. Weeber, A. Dereux, G. Giannoulis, D. Apostolopoulos, H. Avramopoulos, N. Pleros, *IEEE Phot. Technol. Lett.* **2012**, *24*, 1036.

[157] T. R. Buckley, P. Berini, *Opt. Express* **2007**, *15*, 12174.

[158] R. F. Oulton, G. Bartal, D. F. P. Pile, X. Zhang, *New J. Phys.* **2008**, *10*, 105018.

[159] A. V. Krasavin, A. V. Zayats, http://arxiv.org/abs/1510.05931.

[160] A. Degiron, S.-Y. Cho, C. Harrison, N. M. Jokerst, C. Dellagiacoma, O. J. F. Martin, D. R. Smith, *Phys. Rev. A* **2008**, *77*, 021804(R).

[161] H.-S. Chu, E.-P. Li, P. Bai, R. Hegde, *Appl. Phys. Lett.* **2010**, *96*, 221103.

[162] P. Dumon, W. Bogaerts, V. Wiaux, J. Wouters, S. Beckx, J. Van Campenhout, D. Taillaert, B. Luyssaert, P. Bienstman, D. Van Thourhout, R. Baets, *IEEE Phot. Technol. Lett.* **2004**, *16*, 1328.

[163] M. Hill, M. C. Gather, *Nature Photon.* **2014**, *8*, 908.

[164] G. Colas des Francs, P. Bramant, J. Grandidier, A. Bouhelier, J.-C. Weeber, A. Dereux, *Opt. Express* **2010**, *18*, 16327.

[165] D. Yu. Fedyanin, A. V. Krasavin, A. V. Arsenin, A. V. Zayats, unpublished.

[166] A. V. Krasavin, T. P. Vo, W. Dickson, P. M. Bolger, A. V. Zayats, *Nano Lett.* **2011**, *11*, 2231.

[167] Y. B. Khurgin, G. Sun, *Nature Photon.* **2014**, *8*, 468.

[168] D. J. Bergman, M. I. Stockman, *Phys. Rev. Lett.* **2003**, *90*, 027402.

[169] J. Grandidier, G. Colas des Francs, S. Massenot, A. Bouhelier, L. Markey, J.-C. Weeber, C. Finot, A. Dereux, *Nano Lett.* **2009**, *9*, 2935.

[170] C. Garcia, V. Coello, Z. Han, I. P. Radko, S. I. Bozhevolnyi, *Opt. Express* **2011**, *20*, 7771.

[171] J. Grandidier, G. Colas des Francs, S. Massenot, A. Bouhelier, L. Markey, J.-C. Weeber, A. Dereux, *J. Microsc.* **2010**, *239*, 167.

[172] D. Sarid, *Phys. Rev. Lett.* **1981**, *47*, 1927.

[173] J. J. Burke, G. I. Stegeman, T. Tamir, *Phys. Rev. B* **1986**, *33*, 5186.

[174] T. Holmgaard, J. Gosciniak, S. I. Bozhevolnyi, *Opt. Express* **2010**, *18*, 23009.

[175] J. Gosciniak, T. Holmgaard, S. I. Bozhevolnyi, *J. Lightw. Technol.* **2011**, *29*, 1473.

[176] V. S. Volkov, Z. Han, M. G. Nielsen, K. Leosson, H. Keshmiri, J. Gosciniak, O. Albrektsen, S. I. Bozhevolnyi, *Opt. Lett.* **2011**, *36*, 4278.

[177] R. Zektzer, B. Desiatov, N. Mazurski, S. I. Bozhevolnyi, U. Levy, *Opt. Express* **2014**, *22*, 22009.

[178] Y. Binfeng, H. Guohua, C. Yiping, *Opt. Express* **2009**, *17*, 3610.

[179] J. Chen, Z. Li, S. Yue, Q. Gong, *Opt. Express* **2009**, *17*, 23603.

[180] Y. Binfeng, H. Guohua, J. Yang, C. Yiping, *J. Opt. Soc. Am. B* **2009**, *26*, 1924.

[181] D. O'Connor, M. McCurry, B. Lafferty, A. V. Zayats, *Appl. Phys. Lett.* **2009**, *95*, 171112.

[182] H. S. Lee, C. Awada, S. Boutami, F. Charra, L. Douillard, R. Espiau de Lamaestre, *Opt. Express* **2012**, *20*, 8974.

[183] S. Zhu, G. Q. Lo, D. L. Kwong, *Opt. Express* **2012**, *20*, 5867.

[184] Z. Fang, X. Zhang, D. Liu, X. Zhu, *Appl. Phys. Lett.* **2008**, *93*, 073306.

[185] R. F. Oulton, V. J. Sorger, D. A. Genov, D. F. P. Pile, X. Zhang, *Nature Photon.* **2008**, *2*, 496.

[186] H.-S. Chu, P. Bai, E.-P. Li, W. R. J. Hoefer, *Plasmonics* **2011**, *6*, 591.

[187] H.-S. Chu, Y. A. Akimov, P. Bai, E.-P. Li, *J. Opt. Soc. Am. B* **2011**, *28*, 2895.

[188] P. B. Johnson, R. W. Christy, *Phys. Rev. B* **1972**, *6*, 4370.

[189] *Handbook of Optical Constants of Solids* (Ed: E. D. Palik), Academic, New York **1984**.

[190] R. G. Mote, H.-S. Chu, P. Bai, E.-P. Li, *Opt. Comm.* **2012**, *285*, 3709.

[191] M.-Y. Pan, E.-H. Lin, L. Wang, P.-. Wei, *Appl. Phys. A* **2014**, *115*, 93.

[192] Y. Bian, Z. Zheng, Y. Liu, J. Zhu, T. Zhou, *Opt. Express* **2010**, *18*, 23756.

[193] Y. Bian, Z. Zheng, X. Zhao, J. Zhu, T. Zhou, *Opt. Express* **2009**, *17*, 21320.

[194] W. Xu, Z. H. Zhu, K. Liu, J. F. Zhang, X. D. Yuan, Q. S. Lu, S. Q. Qin, *Opt. Lett.* **2015**, *40*, 1603.

[195] C. Donnelly, D. T. H. Tan, *Opt. Express* **2014**, *22*, 22820.

[196] A. Kumar, J. Gosciniak, T. B. Andersen, L. Markey, A. Dereux, S. I. Bozhevolnyi, *Opt. Express* **2011**, *19*, 2972.

[197] T. B. Andersen, Z. Han, S. I. Bozhevolnyi, *Sensors* **2011**, *11*, 1992.

[198] T. B. Andersen, S. I. Bozhevolnyi, L. Markey, A. Dereux, *Opt. Express* **2011**, *19*, 26423.

[199] Z. Fang, H. Qi, C. Wang, X. Zhu, *Plasmonics* **2010**, *5*, 207.

[200] D. O'Connor, A. V. Zayats, *Nature Nanotechnol.* **2010**, *5*, 482.

[201] Y. Li, A. Ma, L. Yang, X. Zhang, *Plasmonics* **2014**, *9*, 71.

[202] G. Magno, M. Grande, V. Petruzzelli, A. D'Orazio, *Sens. Actuat. B – Chem.* **2013**, *186*, 148.

[203] B. Schwarz, P. Reininger, D. Ristanic, H. Detz, A. M. Andrews, W. Schrenk, G. Strasser, *Nat. Commun.* **2014**, *5*, 4085.

[204] D. Ristanic, B. Schwarz, P. Reininger, H. Detz, T. Zederbauer, A. M. Andrews, W. Schrenk, G. Strasser, *Appl. Phys. Lett.* **2015**, *106*, 041101.

[205] J. S. Fakonas, H. Lee, Y. A. Kelaita, H. A. Atwater, *Nature Photon.* **2014**, *8*, 317.

[206] J. S. Fakonas, A. Mitskovets, H. A. Atwater, *New J. Phys.* **2015**, *17*, 023002.

[207] Y.-J. Cai, M. Li, X.-F. Ren, C.-L. Zou, X. Xiong, H.-L. Lei, B.-H. Liu, G.-P. Guo, G.-C. Guo, *Phys. Rev. Appl.* **2014**, *2*, 014004.

[208] F. Ruting, P. A. Huidobro, F. J. Garcia-Vidal, *Opt. Lett.* **2011**, *36*, 4341.

REVIEW